Registration, Atlas Estimation and Variability Analysis of White Matter Fiber Bundles Modeled as Currents

Stanley Durrleman[a,b,d,*], Pierre Fillard[c], Xavier Pennec[a], Alain Trouvé[b], Nicholas Ayache[a]

[a] *Asclepios team project, INRIA Sophia Antipolis Méditerranée, 2004 route des Lucioles, 06902 Sophia Antipolis cedex, France*
[b] *Centre de Mathématiques et Leurs Applications, ENS Cachan, 61 avenue du président Wilson, 94235 Cachan cedex, France*
[c] *Parietal team project, INRIA Saclay-Ile de France, Neurospin Bâtiment 145, 91190 Gif-sur-Yvette, France*
[d] *SCI Institute, University of Utah, 72 S. Central Drive, 84112 Salt Lake City, USA*

Abstract

This paper proposes a generic framework for the registration, the template estimation and the variability analysis of white matter fiber bundles extracted from diffusion images. This framework is based on the metric on currents for the comparison of fiber bundles. This metric measures anatomical differences between fiber bundles, seen as global homologous structures across subjects. It avoids the need to establish correspondences between points or between individual fibers of different bundles. It can measure differences both in terms of the geometry of the bundles (like its boundaries) and in terms of the density of fibers within the bundle. It is robust to fiber interruptions and reconnections. In addition, a recently introduced sparse approximation algorithm allows us to give an interpretable representation of the fiber bundles and their variations in the framework of currents.

First, we used this metric to drive the registration between two sets of homologous fiber bundles of two different subjects. A dense deformation of the underlying white matter is estimated, which is constrained by the bundles seen as global anatomical landmarks. By contrast, the alignment obtained from image registration is driven only by the local gradient of the image.

Second, we propose a generative statistical model for the analysis of a

*Corresponding author
Email address: stanley@sci.utah.edu (Stanley Durrleman)

collection of homologous bundles. This model consistently estimates prototype fiber bundles (called template), which capture the anatomical invariants in the population, a set of deformations, which align the geometry of the template to that of each subject and a set of residual perturbations. The statistical analysis of both the deformations and the residuals describe the anatomical variability in terms of geometry (stretching, torque, etc.) and "texture" (fiber density, etc.).

Third, this statistical modeling allows us to simulate new synthetic bundles according to the estimated variability. This gives a way to interpret the anatomical features that the model detects consistently across the subjects. This may be used to better understand the bias introduced by the fiber extraction methods and eventually to give anatomical characterization of the normal or pathological variability of fiber bundles.

Keywords: Computational Anatomy, fiber bundle, fiber tract, diffusion imaging, diffeomorphic registration, atlas construction, variability analysis, currents

---

1. Introduction

1.1. Analysis of images versus analysis of anatomical structures

Within the framework of Computational Anatomy, one aims at studying the invariance and the variability of anatomical structures across a given population. The estimation of so-called templates gives a representation of the common anatomical features detected in the population. Such templates are used as reference anatomies, for instance for the segmentation and the identification of anatomical structures in new subjects. The analysis of the variability of these typical structures in the population is used to characterize pathologies with respect to normal variations, to find consistent subtypes or to better constrain the segmentation of these structures in images of new subjects. In brain imaging, such an analysis has been proposed for the sulcal lines (Ochiai et al., 2004; Fillard et al., 2007b; Durrleman et al., 2008), the cortex surface in whole or in part (Mangin et al., 2004; Juch et al., 2005; Vaillant et al., 2007) or the subcortical structures (Vaillant et al., 2004; Durrleman et al., 2009b) for instance. Most of these methods focus on the anatomical structures in the grey matter. Much fewer approaches have been proposed for the main structures within the white matter, the neural pathways, although the characterization of their spatial organization is of great

importance, for instance to better understand its relation to the connectivity of the functional areas, or to understand how pathologies like Alzheimer's disease or tumor growths affect the connectivity of the brain and its function.

At the macroscopic level, there is no non-invasive method which allows us a direct measure of the geometry of the neural pathways. Instead, we access a measure of the diffusivity property of the brain, at the voxel level, via diffusion imaging. This is the reason why the variability analysis of the white matter often relies on diffusion images. This includes images of fractional anisotropy (Smith et al., 2006; Goodlett et al., 2008; Faria et al., 2010; Delmaire et al., 2009) or images of tensors (Alexander et al., 2001; Jones et al., 2002; Cao et al., 2005; Zhang et al., 2007; Yeo et al., 2009), for instance. The problem with these approaches is that there is no guarantee that the variability of the measures of diffusivity reflects the variability of the underlying neural pathways. The link between the images of tensors and the anatomy of the neural pathways is rather unclear, especially at fiber crossings. For instance, we do not know to which extent the registration between two images of diffusion correctly aligns the neural pathways.

An alternative approach consists in *estimating* a representation of these neural pathways from the measures of diffusion. The extraction of fibers can be done, for instance, by estimating diffusion tensor images and then using streamline tractography (Basser et al., 2000; Fillard et al., 2007a; Malcolm et al., 2010), with possible uncertainty regions (Jackowski et al., 2005; Staempfli et al., 2006) or by using higher order orientation distribution functions (Descoteaux et al., 2008; Kumar et al., 2009). These algorithms return curves which give an estimation of the location and the orientation of the underlying neural fibers, which are compatible with the measures of diffusivity. Then, fibers may be selected and gathered into anatomically relevant clusters, called fiber bundles in the sequel. This clustering may be done either manually or via the help of registration like in Ziyan & Westin (2009), or via automatic clustering algorithm like in Savadjiev et al. (2008); Wassermann et al. (2010) for instance. These fiber bundles give an estimation of the anatomy of the true underlying neural pathways. The purpose of this paper is to propose a generic method for the analysis of the variability of such fiber bundles, which can be run independently of the algorithms used for their estimation.

On the one hand, methods based on images have the advantage to rely directly on the physical measures and not on tractography and clustering procedure. On the other hand, methods based on the extracted and selected

fiber bundles focus directly on the structures of interest. The two approaches are not equivalent since the anatomical information contained in a set of fiber bundles is not the same than that contained in images. For instance, the fibers do not necessarily follow the largest eigenvalue of the tensors since realistic smoothness constraints are added during tractography. At fiber crossings, the set of fiber bundles takes into account two different labeled directions, thus breaking the isotropy of the tensors in such regions. The clustering of the fibers introduces boundaries between different anatomical structures which are not visible in the images. The estimated fibers give information only in certain regions of space, whereas the images give a dense measure in the whole white matter.

Of course, basing the variability analysis on the estimated fiber bundles raises an important methodological issue. How can one reliably extract and select fiber bundles if one has no idea of their appearance? In other words, the variability analysis is biased by the assumptions and the anatomical priors of the tractography and fiber clustering methods. These priors exactly contains the kind of anatomical information that the variability analysis aims at retrieving. We notice that this criticism holds for any statistical analysis of anatomical structures, which are segmented from anatomical images. Nevertheless, the variability analysis may help, in turn, to highlight and better understand the bias that the extraction and selection methods introduce and eventually may improve the estimation of the true anatomical variability. We consider the proposed variability analysis as an important step toward the final goal which is to use the results of this analysis to improve tractography algorithms, to set up more realistic priors for the selection of the fiber bundles, to strengthen the estimation of the anatomical variability thanks to its correlations with biomarkers and eventually to increase our knowledge of the true anatomical variability. We believe that this approach is more adapted to understand the connectivity of the brain since it is directly based on the anatomical structures of interest: the fiber bundles, and not on the images from which no anatomical information has been selected.

1.2. Metric between fiber bundles

The analysis of the variability of fiber bundles requires the definition of a metric between such fiber bundles, which takes into account the specific geometry of these structures. The metrics proposed so far are based on the correspondence between points or on the correspondence between fibers like in Ding et al. (2003); Corouge et al. (2006); Batchelor et al. (2006); Ziyan

et al. (2007) for instance. However, it has never been shown that individual points on a fiber or individual fibers within a bundle are homologous anatomical structures across a population. The single homologous structure is the fiber bundle itself, considered as a whole. They have names and have been shown to have a functional role for the connexion of different cortical areas. Moreover, different tractography algorithms may retrieve different sets of curves, labeled as the same bundle: the long-range interactions between the starting point and the end point of an individual fiber should not be considered as reliable since the true neural pathway may correspond to the union of several pieces of fibers. By contrast, we think that the estimation of the local orientation of the bundle is a reliable feature, independently of the way these local orientations are connected among themselves. Therefore, a metric between fiber bundles should compare the global shape of the bundles (i.e. its boundaries), should rely on the local orientation of the fibers, should be robust to fiber interruption or reconnection and should not rely on a point or fiber correspondence strategy.

As preliminarily shown in Durrleman et al. (2009a), the metric based on currents seems to be particularly well suited for this purpose. It has been introduced in field of medical imaging in Vaillant & Glaunès (2005); Glaunès (2005); Glaunès et al. (2008) to avoid the need to find point correspondences in feature-based registration as in Chen & Medioni (1991); Besl & McKay (1992); Joshi & Miller (2000) for instance. In the space of currents, the geometrical objects are characterized by their response to any 'exciting' vector field. This gives an indirect way to measure shape dissimilarity without the need for point correspondences. In this setting, a discrete curve is decomposed into a set of unconnected oriented points, called momenta, which encode the local direction of the curves. Therefore, fiber bundles are seen as a collection of oriented points and the metric compares such collections as a whole. The metric is robust to curves interruption and reconnection and to the sampling of the curves.

This metric allows us also to measure differences between bundles in terms of fiber density. Two bundles with the same boundaries but with different fiber densities are distinguishable. This can be used to characterize the residual variability which remains once the fiber bundles are co-registered. Moreover, such residual differences can be easily visualized and then interpreted thanks to the sparse approximation of currents introduced in Durrleman et al. (2009b), which highlights the regions where the fiber density varies.

Besides these advantages, the versatility of the metric on currents opens

up the possibility to deal in a single consistent framework the anatomical structures of both the grey and the white matter, whether they are described by single curves like sulcal lines, by set of curves like fiber bundles or by meshes like subcortical structures of the brain.

1.3. Registration and statistical analysis

The metric between fiber bundles modeled as currents can be used for both registration and statistical analysis. The registration can be achieved by minimizing a criterion which measures in the space of currents the discrepancy between the deformed bundles of the source subject and the bundles of the target subject. The resulting deformation should be able to align the anatomy of the two subjects, namely not only the extracted features but also any anatomical structures contained in the image domain. Therefore, we consider the registration as the search for the "optimal" deformation of the underlying white matter constrained by the position of the fiber bundles. Such a registration may be compared with registration methods which are driven by the image intensity.

The registration is a key tool to analyze the variability of the anatomy of fiber bundles across subjects. The obtained deformations decompose the anatomical differences between two subjects in a geometrical part encoded by one diffeomorphism and a "texture" part encoded by the residual currents (what remains after diffeomorphic registration). The geometrical part captures smooth variations like stretching, shrinking, torque, etc.. The "texture" part captures non-diffeomorphic variations such as change of fiber density or change of topology of the bundles (e.g. the number of branches of a bundle).

Then, registration are embedded into a rigorous statistical framework which allows us to estimate an atlas from a set of fiber bundles extracted from several subjects. By atlas, we mean a template (i.e. a set of prototype bundles), the registration of the template space to the anatomical space of each subject and the residuals (i.e. the difference between the deformed template and the bundles of the considered subject). The template captures the anatomical invariants across the subjects. The deformations capture the geometric variability. The residuals capture the "texture" variability. This description of the variability is not unlike the geometry and texture decomposition in image analysis (Meyer, 2001).

In this paper, we propose to base the statistical estimation of the atlas (template, deformations and residuals) on a generative model similar to the one introduced in Allassonnière et al. (2007); Allassonnière & Kuhn

(2009); Durrleman et al. (2009b). We consider that the observed bundles results from random deformations of an unknown template plus random non-diffeomorphic perturbations in the space of currents. The estimation of the atlas given a collection of homologous fiber bundles is done via A Maximum A Posteriori (MAP) procedure. Principal Component Analysis (PCA) on deformations and residuals lead to a description of the anatomical variability both in terms of the "geometry" and the "texture".

Eventually, thanks to the generative property of the model, one may simulate new synthetic bundles according to the estimated variability. This gives a way to visually represent the variability captured by the model, to estimate how realistic it is and to interpret it. This interpretation should help to better understand the bias introduced by the extraction and selection of the fiber bundles and eventually to highlight the true anatomical variability.

1.4. Paper organization

In Section 2, we will show how the metric on currents can be used to measure dissimilarities between fiber bundles both in terms of geometry and fiber density. In Section 3, we will explain how the metric on currents can be used to drive the registration between two sets of homologous bundles. In Section 4, we will use the registration scheme and the metric on currents to estimate atlases of fiber bundles and to give quantitative measures of the geometric and "texture" variability. In Section 5, numerical experiments will highlight the differences between the alignments of fiber bundles obtained from our registration scheme and the one computed from images. We will also perform the statistical analysis of the fiber bundles extracted on six subjects and will show that it enables to retrieve interesting anatomical information in both the geometric and "texture" part. Eventually, simulation of synthetic bundles will illustrate in an interpretable way the variability captured by the method.

2. Metric between fiber bundles using currents

2.1. Curves tested on vector fields

A fiber bundle is given as a set of curves embedded in the ambient 3D space. We denote $\mathcal{B}$ a generic bundle made of several individual fibers F_i: $\mathcal{B} = \cup_i F_i$. The idea of currents is to characterize the bundle via its response to 'exciting' vector fields. The response of the bundle $\mathcal{B}$ to any vector field

ω (defined in the whole 3D space) is given by the path integral of the vector field along the fibers of the bundle:

$$\mathcal{B}(\omega) = \sum_i \int_{F_i} \omega(x)^t \tau_i(x) dx, \tag{1}$$

where $\tau_i(x)$ denotes the tangent vector of the fiber F_i at the point x (see Fig. 1). In this equation, we suppose that the curves are oriented and have the same orientation. The idea is that the collection of real numbers $\mathcal{B}(\omega)$ for all possible vector fields ω characterizes the geometry of the bundle $\mathcal{B}$. Note that this characterization does not make any strong assumption about the smoothness of the curves: they need only to be orientable and rectifiable, which include both smooth curves and their discretization as polygonal lines.

Mathematically speaking, the bundle is seen as continuous linear map ($\omega \rightarrow \mathcal{B}(\omega)$) from the space of continuous and bounded vector fields ω to the space of real numbers. The usual addition, subtraction and scaling of mappings yields similar operations on fiber bundles.

Given two fiber bundles $\mathcal{B}_1$ and $\mathcal{B}_2$, their sum in the space of currents is defined by the mapping: $(\mathcal{B}_1 + \mathcal{B}_2)(\omega) = \mathcal{B}_1(\omega) + \mathcal{B}_2(\omega)$. The response of the sum of the bundles is equal to the sum of the responses of each bundle, i.e. the sum of the path integral along the fibers of $\mathcal{B}_1$ and of the ones of $\mathcal{B}_2$. Therefore, the addition in the space of currents corresponds to the union of the curves. Similarly, each individual fiber F_i within a bundle $\mathcal{B}$ can be seen as an individual current ($F_i(\omega) = \int_{F_i} \omega(x)^t \tau_i(x) dx$). The bundle is the *union* of all individual fibers $\mathcal{B} = \cup_i F_i$. In the space of currents, the bundle is the *sum* of all the fibers, which leads to $\mathcal{B}(\omega) = \sum_i F_i(\omega)$ as in Eq. (1).

If one changes the orientation of a fiber F_i then the path integral along F_i has the opposite sign. Therefore, the current associated to the fiber F_i with opposite orientation is $-F_i$ ($(-F_i)(\omega) = -F_i(\omega)$). Changing the orientation of a curve gives the opposite current. The union of a curve F_i with itself but with opposite orientation cancels out in the space of current ($F_i - F_i = 0$). A computational way to reduce the density of fibers within a bundle is to add fibers with opposite orientation. The difference between two bundles $\Delta\mathcal{B} = \mathcal{B}_2 - \mathcal{B}_1$ is the union of all the curves of $\mathcal{B}_1$ and $\mathcal{B}_2$ where the orientation of every curve of $\mathcal{B}_1$ has been changed.

The scaling of a bundle by a factor λ is defined as the scaling of the path integral by the same factor: $(\lambda\mathcal{B})(\omega) = \lambda\mathcal{B}(\omega)$. This allows us to define a bundle as a weighted sum of the individual fibers $\mathcal{B} = \sum_i \lambda_i F_i$ such that

$\mathcal{B}(\omega) = \sum_i \lambda_i F_i(\omega)$. This gives more or less weight to each individual fiber within a bundle. In Eq. (1), we assumed that every fiber has the same weight: $\lambda_i = 1$ for all i.

This model of shapes is fully robust to topology changes. If an individual fiber is cut into several pieces, then the union of all these pieces give exactly the same current as the original fiber (i.e. the sum of the integrals along every piece is equal to the integral along the original fiber).

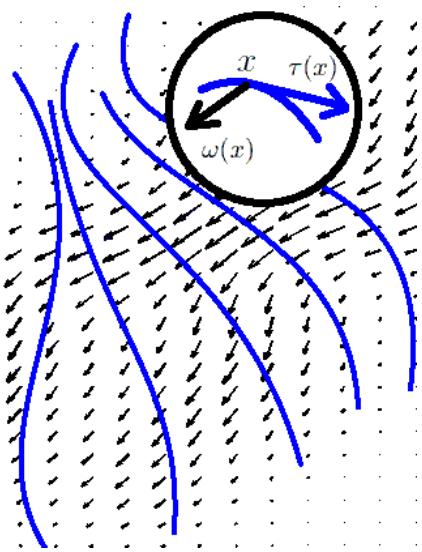

Figure 1: In the framework of currents, curves are tested on vector fields via the path-integral of the vector field along the curves. When one knows the result of this operation for every vector field possible, one gets a characterization of the geometrical object. This indirect way to model shapes embeds shapes into a vector space provided with a metric. If the test space of vector fields has a particular structure, then the distance between two sets of curves has a closed form which does not require to exhaustively explore the whole set of possible vector fields.

2.2. Correspondence-free distance between fiber bundles

Let $\mathcal{B}_1$ and $\mathcal{B}_2$ be two fiber bundles and $\Delta\mathcal{B} = \mathcal{B}_2 - \mathcal{B}_1$ their difference as currents. For a given vector field ω, $\Delta\mathcal{B}(\omega) = \mathcal{B}_2(\omega) - \mathcal{B}_1(\omega)$ is the difference of the path integrals of ω along the two bundles. To measure the dissimilarity between the two bundles, one wants to find the vector field ω which maximizes this difference, namely by computing:

$$\|\Delta\mathcal{B}\| = \sup_{\|\omega\|_\infty = 1} |\Delta\mathcal{B}(\omega)| \,. \tag{2}$$

The supremum guarantees that the norm vanished ($\|\Delta\mathcal{B}\| = 0$) if and only if $\Delta\mathcal{B}(\omega) = 0$ for all ω. This means that we cannot find any vector fields ω which can distinguish between the two integrals $\mathcal{B}_1(\omega)$ and $\mathcal{B}_2(\omega)$:

the curves along which one integrates ω coincide (up to a set of null measure) and the two bundles are perfectly superimposed. Note that this is the standard definition of the operator norm of the linear form $\Delta\mathcal{B}$ on the space of continuous bounded vector fields[1].

For the sake of simplicity, we assume now that the two bundles consist of a single individual fiber each. If these two curves do not intersect, the vector field ω_{12} which maximizes Eq. (2) (up to a normalization constant) is such that $\omega_{12}(x)$ is equal to the tangent $\tau_2(x)$ at every point x of the second curve and $\omega_{12}(x)$ is equal to the tangent $-\tau_1(x)$ at every point x of the first curve. In this case, the value of the maximum is proportional to the sum of the length of both curves. If the two curves intersect, the current $\Delta\mathcal{B}$ equals zero on the parts of the curves which overlap. In this case, the maximum in Eq. (2) is the sum of the length of both curves minus the length of the overlapping part. Therefore, this dissimilarity metric measures how much the two curves overlap.

This dissimilarity metric does not seem to be very useful and obviously is not well-posed from a numerical point of view: the metric captures the shape similarity only if the curve are perfectly superimposed. If a curve is translated then the distance between the translated curve and the original one is constant, independently of the magnitude of the translation. This comes from the fact that we do not impose any spatial smoothness constraints on the vector fields, so that we can always find one which perfectly interpolates the tangents of the two curves as long as these curves do not overlap. To overcome this issue, we restrict the vector fields on which we test the curves (in Eq. (1)) to have smooth spatial variations. To do this, we choose vector fields as the convolutions between any square integrable vector fields and a smoothing kernel K^W. The kernel plays the role of a low-pass filter on the spatial frequencies of the vector fields. In this work, we will use a Gaussian kernel: $K^W(x,y) = \exp(-|x-y|^2/\lambda_W^2)\mathrm{I}$ for every point x, y and where I stands for the 3-by-3 identity matrix.

A rigorous construction of a test space W of such smooth vector fields can be done in the framework of reproducible kernel Hilbert spaces (RKHS)

[1] If A is a definite positive matrix, $\sup_{\|X\|=1} \|AX\|$ is equal to the largest eigenvalue of A, namely its spectral norm, if $\|\|$ denotes the usual Euclidean norm on $\mathbb{R}^n$. Here ΔB is an infinite dimensional linear operator but the definition of such norms still holds. In Eq. (2), we used the supremum norm of vector fields. In the following, we will use a regularized L^2 norm instead.

(see Aronszajn (1950); Glaunès (2005); Durrleman (2010) for more details). In this context, one may show that the vector field ω_{12} which maximizes $\sup_{\|\omega\|_W=1} |\Delta\mathcal{B}(\omega)|$ (where $\|\omega\|_W$ stands for the norm of the vector field in the RKHS) is given by $\omega_{12}/\|\omega_{12}\|_W$ where:

$$\omega_{12}(x) = \int_{\mathcal{B}_2} K^W(x,y)\tau_2(y)dy - \int_{\mathcal{B}_1} K^W(x,y)\tau_1(y)dy \tag{3}$$

This means that ω_{12} is the convolution of every tangent of the second curve minus the convolution of every tangent of the first curve, as illustrated in Fig. 2. Note that this continuous formulation holds for both continuous curves and polygonal lines, and that, in this last case, the arc-length integrals are independent of the distribution of the samples. The kernel can be seen as a way to define an "area of influence" of the curve around its location, which is reflected in the *dense* vector field ω_{12} build from *singular* curves. In the limit of a small spatial scale $\lambda_W \to 0$, $\omega_{12}(x)$ vanishes everywhere but on $\mathcal{B}_1$ and $\mathcal{B}_2$ where it equals $-\tau_1(x)$ and $\tau_2(x)$ respectively. In this case, the highest frequencies of the vector fields are not penalized and the metric considers that the curves are distinct as long as they do not intersect, like when we considered the supremum norm instead of the RKHS one in Eq. (2). As λ_W increases, the interpolating vector field ω_{12} can less and less interpolate the tangents of the two curves and the two curves interact as soon as they are within a typical distance of λ_W. At the limit of a very large scale $\lambda_W \to \infty$, the kernel $K^W(x,y)$ is almost constantly equal to 1 and the interpolating vector field $\omega_{12}(x)$ is constant and equals to $\int_{\mathcal{B}_2}\tau_2(y)dy - \int_{\mathcal{B}_1}\tau_1(y)dy$, namely the difference between the length of the two curves. It is as if the two curves are perfectly superimposed: at such scales, one does not see any differences between the two curves, which tend to coincide in the space of currents. In Fig. 3, we show the impact of the spatial scale λ_W on the interpolating vector field.

The squared distance between the two curves is given by $d(\mathcal{B}_1,\mathcal{B}_2)^2 = \Delta\mathcal{B}(\omega_{12}) = \mathcal{B}_2(\omega_{12}) - \mathcal{B}_1(\omega_{12}) = \int_{\mathcal{B}_2}\omega_{12}(x)^t\tau_2(x)dx - \int_{\mathcal{B}_1}\omega_{12}(x)^t\tau_1(x)dx$. Given the expression of ω_{12} in Eq. (3), we get:

$$\begin{aligned} d(\mathcal{B}_1,\mathcal{B}_2)^2 = \int_{\mathcal{B}_1}\int_{\mathcal{B}_1} \tau_1(x)^t K^W(x,y)\tau_1(y)dxdy + \int_{\mathcal{B}_2}\int_{\mathcal{B}_2} \tau_2(x)^t K^W(x,y)\tau_2(y)dxdy \\ - 2\int_{\mathcal{B}_1}\int_{\mathcal{B}_2} \tau_1(x)^t K^W(x,y)\tau_2(y)dxdy \end{aligned} \tag{4}$$

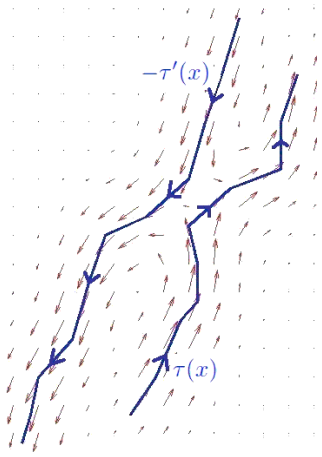

Figure 2: Distance between two curves $\mathcal{B}_1$ and $\mathcal{B}_2$. One builds the current $\mathcal{B}_1 - \mathcal{B}_2$ by inverting the orientation of $\mathcal{B}_2$ and building the union of the tangents of both curves. The best interpolating vector field $\omega_{12}(x)$ is displayed (i.e. the convolution of all the tangents of the $\mathcal{B}_1$ and $-\mathcal{B}_2$) with the two original curves superimposed. The distance between both curves is given by the integration of this vector field along the curve $\mathcal{B}_1$ and the curve $-\mathcal{B}_2$: $\|\mathcal{B}_1 - \mathcal{B}_2\|^2 = \int_{\mathcal{B}_1} \omega_{12}(x)^t \tau_1(x) dx - \int_{\mathcal{B}_2} \omega_{12}(x)^t \tau_2(x) dx$. If the polygonal lines are approximated with a finite number of momenta, these integrals become finite sums over the segments of the lines.

The first term in Eq. (4) involves only the first curve. The second term involves only the second curve. The third term is an interaction term between the two curves. If λ_W tends to zero, this third term vanishes for distinct curves.

This distance is a norm which comes from an inner-product, as shown in (Glaunès, 2005; Durrleman, 2010) for instance. For every current $\mathcal{B}$, the norm of the current is defined as $\|\mathcal{B}\|_{W^*} = \sup_{\|\omega\|_W=1} |\mathcal{B}(\omega)|$, where W^* denotes the space of currents (dual of the space of vector field W). Then, the first term in Eq. (4) is equal to $\|\mathcal{B}_1\|^2_W$, the second term equals $\|\mathcal{B}_2\|^2_W$ and the third term equals $-2\langle \mathcal{B}_1, \mathcal{B}_2 \rangle_{W^*}$. Eventually, Eq. (4) may be written as:

$$d(\mathcal{B}_1, \mathcal{B}_2)^2 = \|\mathcal{B}_2 - \mathcal{B}_1\|^2_{W^*} = \|\mathcal{B}_1\|^2_{W^*} + \|\mathcal{B}_2\|^2_{W^*} - 2\langle \mathcal{B}_1, \mathcal{B}_2 \rangle_{W^*}.$$

Moreover, we have $\Delta\mathcal{B}(\omega_{12}) = \|\omega_{12}\|^2_W = \|\Delta\mathcal{B}\|^2_{W^*}$, which shows that there is an isometric map between the interpolating vector field ω_{12} and the current $\Delta\mathcal{B}$. The interpolating vector field which achieves the supremum $\sup_{\|\omega\|_W=1} |\Delta\mathcal{B}(\omega)|$ always exists and is unique.

Now, if the bundles $\mathcal{B}_1$ and $\mathcal{B}_2$ do not consist of single individual fibers, but a set of N fibers F^1_i and M fibers F^2_i instead, then they are written as currents: $\mathcal{B}_1 = \sum_{i=1}^N F^1_i$ and $\mathcal{B}_2 = \sum_{i=1}^M F^2_i$ and their distance is measured

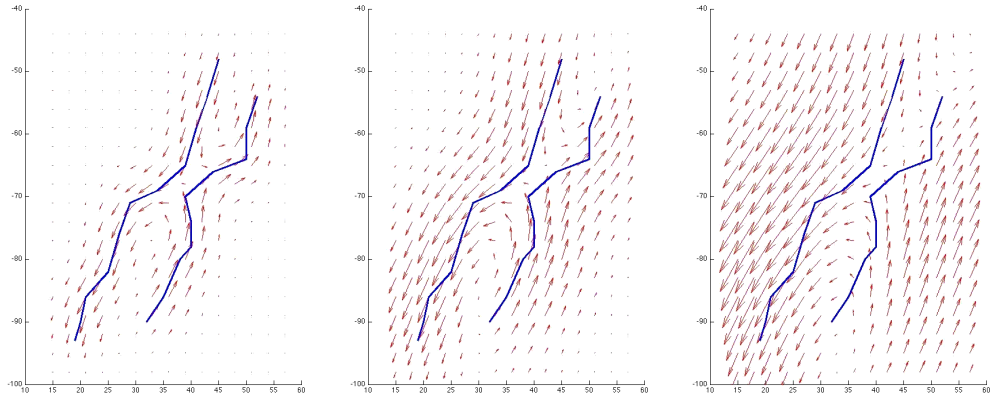

$\lambda_W = 5$ $\lambda_W = 10$ $\lambda_W = 20$

Figure 3: Impact of the kernel on the distance between two curves $\mathcal{B}_1$ and $\mathcal{B}_2$. The vector field $\omega_{12}(x)$ associated to the current $\mathcal{B}_2 - \mathcal{B}_1$ is shown, with the two original curves superimposed. This is the vector field in the test space W which best separates the two curves. The result is shown for 3 different standard deviations of the Gaussian kernel: $\lambda_W = 5, 10$ and 20. For small λ_W, the vector field can vary fast enough, so that it can follows almost every small details of the curves and therefore almost perfectly interpolates between the directions of the curves: the two curves are almost orthogonal in the space of currents ($\arccos\left(\frac{|\langle L_1, L_2\rangle_{W^*}|}{\|L_1\|_{W^*}\|L_2\|_{W^*}}\right) = 85^\circ$ for $\lambda_W = 5$). For large λ_W, the highest spatial frequencies are excluded from W: the vector field cannot adapt to the small-scale variations of the curves: the two curves become more and more aligned in the space of currents ($\arccos\left(\frac{|\langle L_1, L_2\rangle_{W^*}|}{\|L_1\|_{W^*}\|L_2\|_{W^*}}\right) = 65^\circ$ for $\lambda_W = 10$ and 38° for $\lambda_W = 20$).

by:

$$\left\|\sum_{i=1}^{N} F_i^1 - \sum_{i=1}^{M} F_i^2\right\|_{W^*}^2 = \left\|\sum_{i=1}^{N} F_i^1\right\|_{W^*}^2 + \left\|\sum_{i=1}^{M} F_i^2\right\|_{W^*}^2 - 2\left\langle \sum_{i=1}^{N} F_i^1, \sum_{i=1}^{M} F_i^2 \right\rangle_{W^*}$$
$$= \sum_{i=1}^{N}\sum_{j=1}^{N} \left\langle F_i^1, F_j^1\right\rangle_{W^*} + \sum_{p=1}^{M}\sum_{q=1}^{M} \left\langle F_p^2, F_q^2\right\rangle_{W^*} - 2\sum_{i=1}^{N}\sum_{q=1}^{M} \left\langle F_i^1, F_q^2\right\rangle_{W^*} \quad (5)$$

where the inner-product between two individual fibers F_p and F_q is given as:

$$\langle F_p, F_q\rangle_{W^*} = \int_{F_p}\int_{F_q} \tau_p(x)^t K^W(x,y)\tau_q(y)dxdy \quad (6)$$

Eq. (5) is exactly Eq. (4) where $\int_{\mathcal{B}_1}\cdots$ is replaced by $\sum_{i=1}^{N}\int_{F_i^1}\cdots$ and

$\int_{\mathcal{B}_2} \cdots$ by $\sum_{i=1}^{M} \int_{F_i^2} \cdots$. This equation shows that the distance between two bundles can be computed even if the number of fibers within each bundle is different. This distance does not assume either homologous points or homologous fibers between bundles. It considers the "shape" of the bundle globally.

Eventually, to compare two bundles we only need to compute the closed form in Eq. (5), thus avoiding to search for the supremum in Eq. (2) by exploring the whole set of vector fields in W. It is not needed either to store the interpolating vector field ω_{12}.

2.3. Discretization of fiber bundles

From a numerical point of view, the individual fibers extracted from DTI are given as polygonal lines (set of connected points which build segments). All the points x along one segment share the same tangent vector: $\tau(x) = \tau$. This segment (which can be considered itself as a current) may be approximated by a Dirac delta current: δ_c^τ where c denotes the center of mass of the segment (or any fixed point on the segment). The Dirac delta current is defined via its action on any vector fields ω by: $\delta_c^\tau(\omega) = \omega(c)^t\tau$. This approximation means that we replace the integral along the segment C: $\int_C \omega(x)^t\tau(x)dx$ by the single value $\omega(c)^t\tau$. The oriented point (c, τ) is called a momentum. The magnitude of the momentum $|\tau|$ encodes the total length of the segment (see Fig. 4).

This approximation decomposes a fiber bundle into a set of unconnected oriented points (momenta) (x_i, τ_i), which describes the bundle as a set of local orientations. The associated current is given as: $\mathcal{B} \sim \sum_i \delta_{x_i}^{\tau_i}$, where each momenta (x_i, τ_i) approximates a segment in the bundle $\mathcal{B}$, independently of the fiber it actually belongs to. In the space of currents, the long-range connectivity between point is lost and only the local orientation is taken into account.

The inner-product between two Dirac delta currents is given as: $\left\langle \delta_x^\alpha, \delta_y^\beta \right\rangle_{W^*} = \alpha^t K^W(x, y)\beta$ (where K^W is the smoothing kernel), therefore the distance between the approximation of two bundles $\mathcal{B}_1 = \sum_{i=1}^{N_1} \delta_{x_i}^{\tau_i}$ and $\mathcal{B}_2 = \sum_{i=1}^{N_2} \delta_{y_i}^{\zeta_i}$ is

given as:

$$d(\mathcal{B}_1,\mathcal{B}_2)^2 = \sum_{i=1}^{N_1}\sum_{j=1}^{N_1}\tau_i^t K^W(x_i,x_j)\tau_j + \sum_{p=1}^{N_2}\sum_{q=1}^{N_2}\zeta_p^t K^W(y_p,y_q)\zeta_q - 2\sum_{i=1}^{N_1}\sum_{q=1}^{N_2}\tau_i^t K^W(x_i,y_q)\zeta_q \quad (7)$$

We notice that this approximation consists in replacing the continuous integrals in Eq. (5) by their Riemann sums. The error of this approximation tends to zero as the sampling of the curves become finer and finer. This shows that this distance is robust to any re-sampling of the curves, which does not increase the magnitude of the segments.

If the number of samples are small, one can use directly the formula in Eq. (7), to compute the distance between the bundles. However, this computation is of complexity $\mathcal{O}(N_1^2 + N_2^2 + N_1N_2)$. In real applications, one needs optimization strategies to decrease this complexity. Optimizations based on Multipole Approximation (Glaunès, 2005) or on linearly spaced grids and FFTs (Durrleman, 2010, Chap. 2) turn this quadratic complexity into an almost linear one, thus yielding an efficient numerical framework for intensive computations on currents. For instance, the vector fields displayed on Fig. 3 are sampled on a regular lattice, thus being encoded by an image of vector. Similarly, we can project the segments of the curves to the nodes of the lattice and sample the kernel on this lattice, thus leading to two images of vectors. Then, the computation of the norm of currents involves only 3D-FFTs and multiplication between images of vectors as detailed in (Durrleman, 2010, Chap. 2).

2.4. Sparse Approximation of Fiber Bundles

The discrete approximation of a fiber bundle in terms of the sum of Dirac delta currents as previously introduced is not always optimal. Indeed, this representation may be redundant at the scale of analysis given by the spatial scale of the kernel λ_W. Because of this smoothing kernel, two segments which are much closer than λ_W are almost undistinguishable in the space of currents. Indeed, the action of any vector field ω on the current $\delta_x^\alpha + \delta_y^\beta$ gives: $\omega(x)^t\alpha + \omega(y)^t\beta$. If the distance between x and y is much smaller than λ_W, then the vector field ω is almost constant in this neighborhood (its spatial variations cannot be much smaller than λ_W by construction) and

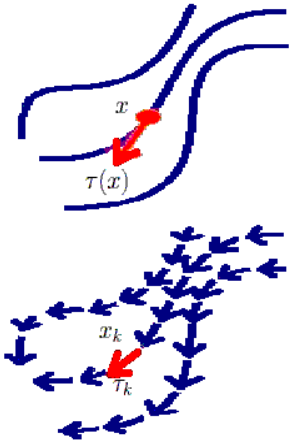

Figure 4: Both continuous and discrete shapes are handled in the same space of currents. In the continuous form, smooth curves are decomposed into the infinite set of their tangents. If curves are sampled, they can be approximated by a finite set of oriented points (called momenta) encoding each segment. The integral of a vector field ω along the smooth curve (i.e. a continuous current) is given as $L(\omega) = \int_L \omega(x)^t \tau(x) dx$. For the discrete approximation, this integral becomes a finite sum $L(\omega) = \sum_k \omega(x_k)^t \tau_k$. The discrete current converges to the continuous one as the sampling of the curves becomes finer and finer. This approximation transforms any set of curves into a cloud of unconnected oriented points.

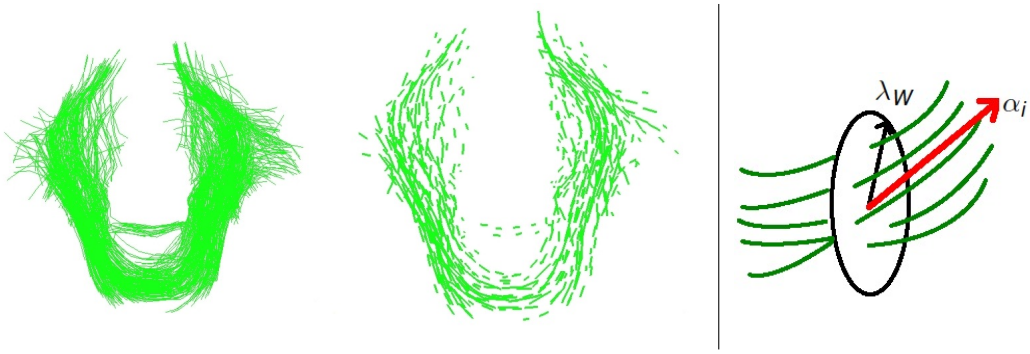

Figure 5: **Left:** A white matter fiber bundle and its sparse approximation at the scale $\lambda_W = 3$mm (the diameter of the data is 100mm) and for an approximation error of 5% of the variance. For visualization purpose, the segments representing estimated momenta are scaled by 0.1. The compression ratio (measured by the number of momenta) is greater than 85%. As illustrated on the **right**, this approximation integrates the local redundancy of the information at the scale λ_W. It approximates the curves which go through every patch of size λ_W by one momentum. The momentum encodes the sum the tangents (taking orientation into account: two curves which go through the patch in opposite direction would cancel out), its magnitude encodes the local redundancy of the initial representation.

$\omega(x)^t\alpha + \omega(y)^t\beta$ may be well approximated by $\omega\left(\frac{x+y}{2}\right)^t(\alpha+\beta)$. This means that the current $\delta_x^\alpha + \delta_y^\beta$ may be approximated by a single momentum $(\frac{x+y}{2}, \alpha+\beta)$ corresponding to the Dirac delta current $\delta^{\alpha+\beta}_{(x+y)/2}$. Given a whole set of momenta, the idea is to approximate the momenta located into every patch of size λ_W by a single momenta (see Fig. 5), thus adjusting the complexity

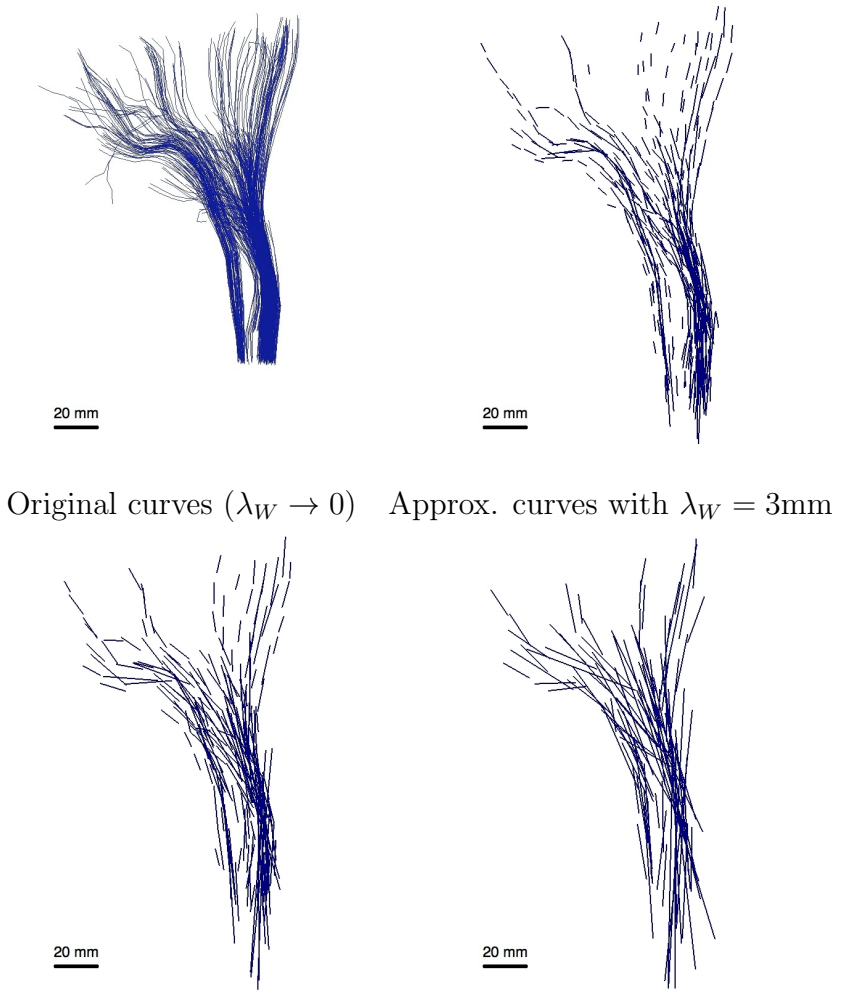

Figure 6: An instance of the corticospinal tract (lateral view) and its sparse approximation for different scale λ_W and a fixed approximation error. The greater λ_W, the more redundant the original representation at the scale λ_W, the sparser the approximation. So, as λ_W increases, the sparse representation tends to have fewer momenta, but with larger magnitudes. The length of the momenta is related to the sum of the length of all the pieces of curves which intersect its 'area of influence' of radius λ_W. Since this total length may be very large (due the high density of fibers in some areas), we scaled the momenta to 0.1 for visualization purposes.

of the representation to the spatial scale of analysis (i.e. its resolution).

The matching pursuit algorithm for currents introduced in Durrleman et al. (2009b) is a generic implementation of this idea. It allows us to estimate a small set of momenta which approximates a given discrete current at any accuracy (the accuracy being measured by the current norm of the difference between the approximated bundle and the original one). The algorithm estimates both the location x and the vector coefficient τ of the momenta. The magnitude of the estimated momenta integrates the redundancy of the initial representation at the scale λ_W (see Fig. 5-right). We say that this approximation is a 'sparse representation' of the current. In Fig. 6, we show such approximations for a fixed numerical error and for different spatial scales λ_W. This illustrates how this spatial scale determines the 'resolution' at which a fiber bundle is seen as a current.

Given a set of 6 fiber bundles like the one shown in Fig. 5, this algorithm enables to achieve a compression ratio of 85% (ratio between the number of estimated momenta and the number of original momenta, i.e. the number of segments) while guaranteeing an approximation error below 5% of the variance of the dataset.

This sparse approximation will be used in the following to give an interpretable representation of linear combination of currents, like the modes of variations estimated from a set of homologous bundles for instance. We will see that such modes are given as a linear combination of all the momenta of all subjects involving both positive and negative weights. The representation of such mode is the union of all segments in the database which have been scaled and whose orientation has been changed in case of negative weight. This representation is difficult to interpret. By contrast, the sparse approximation of this mode integrates the weighted sum in every patch of size λ_W. As a consequence, if the effect of the mode is to decrease the density of fibers by adding momenta with opposite direction that of the bundle, then the sparse representation of the mode will really look like a bundle with a smaller fiber density contrary to the initial representation. Fig. 7 is an illustration of this idea.

Therefore, the sparse approximation is of great interest not only to compress and make tractable the following algorithms on currents (by reducing the number of momenta and hence the complexity of the computation of the norm in Eq. (7)) but also to give interpretable results.

To conclude, the metric on currents is sensitive to two kinds of geometric differences. First, as illustrated in Fig. 3, the metric is sensitive to the geom-

etry of the bundles, mainly their respective positions in space, the location of their boundaries, the spatial repartition of the fibers within the bundles. Second, it is also sensitive to the fiber density. The first aspect of the metric will be used to drive diffeomorphic registration between fiber bundles. The second aspect will be used to analyze the residual variability in terms of fiber density between registered fiber bundles.

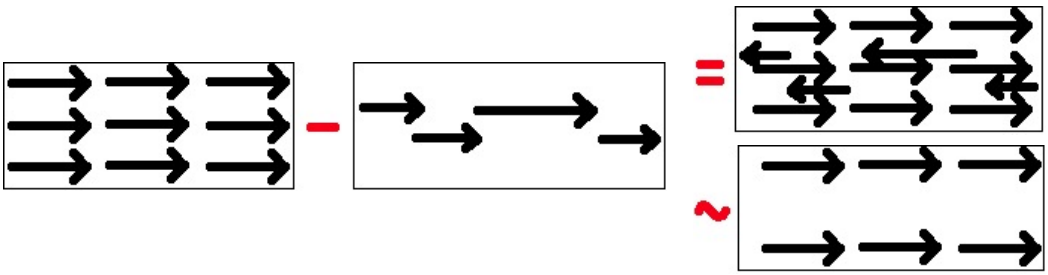

Figure 7: The difference between two currents given as a set of momenta (oriented points) is the union of all the momenta where the orientation of the second ones has been inverted (top right panel). The sparse approximation of this difference locally integrates the positive and negative contributions: it leads to a visual representation of the difference which is interpretable in terms of a decrease of the density of momenta (bottom right panel). This will be used to describe the residual variability of fiber bundles which remains once the bundles have been registered.

3. Registration of fiber bundles driven by the metric on currents

3.1. Mapping between sets of fibers

The purpose of this section is to use the metric on currents to drive the registration between fiber bundles. This registration inherits from the same properties as the metric itself. In particular, it only needs the definition of homologous bundles and not homologous points or fibers. Let $\mathcal{B}_1, \ldots, \mathcal{B}_N$ be N labeled fiber bundles extracted from the DTI of a given subject and $\mathcal{B}'_1, \ldots, \mathcal{B}'_N$ the homologous fiber bundles extracted from the images of another subject (we suppose that the images have been rigidly aligned beforehand). We suppose that fibers within each bundle and across individuals are oriented in a consistent way. Our purpose is to find the most probable (in a sense to be defined) deformation of the underlying white matter which enables to align these two sets of homologous bundles. Let ϕ be a deformation of the underlying $3D$ space. This deformation carries in space the

fibers of the bundle $\mathcal{B}_i$ to $\phi(\mathcal{B}_i)$ (the union of the geometrical deformation of every individual fibers). Then, we want to find the deformation ϕ so that the discrepancy between the deformed bundles $\phi(\mathcal{B}_i)$ and the target bundles $\mathcal{B}'_i$ is minimized. This discrepancy can be measured via: $\sum_{i=1}^{N} \|\phi(\mathcal{B}_i) - \mathcal{B}'_i\|^2_{W^*}$, where each norm is the norm on currents between the deformed source bundle and the target bundle. Let $\mathrm{Reg}(\phi)$ be a measure of the smoothness of the deformation. We define the matching criterion as a trade-off between regularity and fidelity-to-data (weighted by the scalar parameter γ):

$$E(\phi) = \sum_{i=1}^{N} \|\phi(\mathcal{B}_i) - \mathcal{B}'_i\|^2_{W^*} + \gamma \mathrm{Reg}(\phi) \tag{8}$$

To make sense of Eq. (8), we need to precise what is the current associated to $\phi(\mathcal{B}_i)$. For the reasons discussed in the next section, we suppose that the deformation ϕ is a diffeomorphism of the 3D space (one-to-one and smooth map with smooth inverse). Then, if ω is a vector field, a change of variable in Eq. (1) shows that the integration of ω along the deformed fibers of the bundle $\phi(\mathcal{B}_i)$ is equal to the integration along the original fibers of $\mathcal{B}_i$ of the vector field $\phi^*\omega(x) = (d_x\phi)\omega(\phi(x))$ where $d_x\phi$ denotes the Jacobian matrix of the diffeomorphism ϕ at point x. This shows that the deformed bundle $\phi(\mathcal{B})$ can still be considered as a current, as the mapping $\omega \to \mathcal{B}(\phi^*\omega)$. Therefore, the current associated to the deformed bundle, denoted $\phi_*\mathcal{B}$, is defined by: $\phi_*\mathcal{B}(\omega) = \mathcal{B}(\phi^*\omega)$. If δ_x^τ is a Dirac delta current encoding an oriented point (x, τ) then standard computations show that $\phi_*\delta_x^\tau = \delta_{\phi(x)}^{d_x\phi\tau}$: the point x is transported into $\phi(x)$ and the direction τ is deformed according the Jacobian matrix into $d_x\phi\tau$.

As explained in Section 2.3 and 2.4, the bundles $\mathcal{B}_i$ are approximated into a finite combination of momentum of the form: $\tilde{\mathcal{B}}_i = \sum_k \delta_{x_k}^{\tau_k}$ (i.e. a cloud of unconnected oriented points). Therefore, in Eq (8) the current $\phi(\tilde{\mathcal{B}}_i)$ (now denoted $\phi_*\tilde{\mathcal{B}}_i$) is still a finite sum of momenta: $\phi_*\tilde{\mathcal{B}}_i = \sum_k \delta_{\phi(x_k)}^{d_{x_k}\phi\tau_k}$. As a consequence, one can still use Eq. (7) to compute the norm in the matching criterion in Eq. (8) by replacing the momenta (x_i, τ_i) of the moving bundle by the momenta $(\phi(x_i), d_{x_i}\phi\tau_i)$.

This allows us to write now the matching criterion (8) in its most general form as:

$$E(\phi) = \sum_{i=1}^{N} \|\phi_*\mathcal{B}_i - \mathcal{B}'_i\|^2_{W^*} + \gamma \mathrm{Reg}(\phi), \tag{9}$$

where now $\mathcal{B}_i$ can denote either a set of continuous curves, any finite sums of Dirac Delta currents, like the approximation of continuous curves (Sec. 2.3), any weighted sum of such approximations, like the empirical mean of fiber bundles (since any weighted sum $\sum_k w_k \delta_{x_k}^{\alpha^k}$ can be written as a simple sum by weighting the momenta: $\sum_k \delta_{x_k}^{w_k \alpha^k}$) or the sparse approximation of such sums (Sec. 2.4) for instance.

3.2. Criterion minimization in the framework of large diffeomorphic deformations

We choose to optimize the criterion in Eq. (9) over the diffeomorphisms which result from the integration of a time-varying speed vector field, since it has been shown that this framework interfaces well with the metric on currents either for curve registration (Glaunès et al., 2008; Durrleman et al., 2008) or for surface registration (Vaillant & Glaunès, 2005; Durrleman et al., 2009b). The considered diffeomorphisms are solution at time $t = 1$ of the flow equation: $\dot{\phi}_t(x) = v_t(\phi_t(x))$, where $v_t(x)$ for $t \in [0, 1]$ is the a dense $3D$ vector field which gives the speed of a particle at time t and location x. As for the currents, we enforce this speed field to result from a convolution between a squared integrable vector field and a smoothing kernel, in the framework of RKHS. The smoothing kernel determines the typical spatial scale at which the diffeomorphism moves points in a correlated manner. In our applications, we choose a Gaussian kernel with standard deviation λ_V: $K^V(x, y) = \exp(-|x - y|^2 / \lambda_V^2)\mathrm{I}$. We denote $\mathcal{G}_V$ the set of all the diffeomorphisms which result from the integration of the flow equation for all possible time-varying vector fields v_t in the RKHS determined by the kernel K^V. We define the regularity of the deformation $\mathrm{Reg}(\phi)$ in Eq. (9) as the total kinetic energy of the deformation: $\mathrm{Reg}(\phi) = \int_0^1 \|v_t\|_V^2 \, dt$ where $\|v_t\|_V$ denotes the Sobolev norm associated to the kernel K^V.

It has been shown in Glaunès (2005) that the diffeomorphism which minimizes the criterion in Eq. (9) among all the diffeomorphisms in $\mathcal{G}_V$ is parameterized by a time-varying speed vector field v_t which is of the form $v_t(x) = \sum_i K^V(x, x_i(t))\alpha_i(t)$, where x_i denotes either every sample of the moving bundles (if $\mathcal{B}_i$ is a set of polygonal lines) or the localization of the Dirac delta currents (if $\mathcal{B}_i$ is a finite sum of Dirac delta currents). These points move according to the flow equation: $\dot{x}_i(t) = v_t(x_i(t))$ with $x_i(0) = x_i$ and $\alpha_i(t)$ is a set of time-varying $3D$-vectors. As a consequence, the minimizing diffeomorphism is entirely determined by the time-varying vectors $\alpha_i(t)$. The gradient of the criterion in Eq. (9) with respect to these variables

is computed as explained in Glaunès (2005); Durrleman (2010). Then, the registration is computed via a gradient descent scheme.

As the result, the minimizing diffeomorphism is geodesic, in the sense that the estimated time-varying vectors $\alpha_i(t)$ are the ones which minimize $\mathrm{Reg}(\phi)$ among all possible flows which reaches the final diffeomorphism ϕ (since the fidelity-to-data term depends only on this final diffeomorphism and not on the flow which enables to reach it). As a consequence, this minimizing diffeomorphism is entirely determined by its initial speed vector field at time $t = 0$, or equivalently the initial momentum $(x_i, \alpha_i(0))$ (Miller et al., 2002; Vaillant et al., 2004). These initial momenta can be seen as the tangent-space representation of the diffeomorphism by analogy with finite-dimensional Riemannian geometry (Pennec et al., 2006). This tangent-space representation will be used in the next section to perform statistics on diffeomorphisms.

3.3. Diffeomorphic deformations and residuals

In this registration framework, we supposed that the deformation is a diffeomorphism of the space (smooth, one-to-one deformation of the 3D space with smooth inverse). The spatial variations are controlled by the parameter λ_V. For large scale λ_V (compared to the scale of the structures), the considered deformations are almost rigid: only translations and rotations are retrieved. On the contrary, smaller λ_V allows highly non-linear deformations with small-scaled variations (making also greater the cost of a large-scale deformation).

For pure registration purposes, one want to find the best possible alignment between fiber bundles. To achieve such aggressive registration, one wants to favor small scale of deformations λ_V. This parameter must be adjusted to the scale at which one wants the deformation to integrate different spatial constraints, since points at a distance much greater than λ_V will have uncorrelated motions.

The diffeomorphism may align the geometry of the fiber bundles, namely their position, their boundaries and the repartition of the fibers within the bundles. But by nature, such deformations cannot discount for non-diffeomorphic differences such as different fiber densities, changes of topology (fiber bundles with different numbers of branches for different subjects) or even small-scale variations compared to the scale λ_V. In this case, the diffeomorphism which minimizes the registration criterion in Eq. (9) cannot make the discrepancy term ($\|\phi_{i*}\mathcal{B}_i - \mathcal{B}'_i\|_{W^*}$) to decrease close to zero, since the norm on currents is still sensitive to the mis-alignment in terms of fiber densities. The

spatial scale of deformation λ_V along with the trade-off between regularity and fidelity-to-data γ and the spatial sensitivity of the norm of currents λ_W (whose effects have been shown in Fig. 6) determines the balance between the geometrical differences discounted by the diffeomorphism and the differences that are left in the residual current: $\varepsilon_i = \mathcal{B}'_i - \phi(\mathcal{B}_i)$.

In the context of statistical analysis, too aggressive deformations are not desirable since they tend to capture all the information into the geometrical part. They are likely to over-fit the observations, meaning that the analysis of the deformations is unlikely to detect reproducible features across the subjects but rather features specific to each individual. Too rigid deformations are not desirable either, since they tend to leave all the interesting anatomical differences in the residuals. The analysis of these residuals, which would mix information of different kinds and scales, would be particularly difficult. By contrast, we think that the best trade-off (in the sense of the predictive power of the model for instance) is between these two extreme configurations. Deformations are considered as a way to decompose the anatomical differences between two subjects into two terms: the geometrical term encoded in the deformation and the "texture" term encoded in the residuals. The impact of the registration parameters on the decomposition geometry/residuals has been illustrated in Durrleman et al. (2008). The statistical analysis on real dataset with manually fixed parameters will show that both terms may reveal interesting anatomical features.

4. Group-wise statistics of fiber bundles

4.1. Generative statistical model of fiber bundles and its estimation

In this section, we extend the pairwise comparison of anatomies based on registration to group-wise statistics. For the sake of simplicity, we focus here only on a single fiber bundle extracted from images of several subjects. The method straightforwardly applies if several bundles are extracted. In that case, one has one single deformation and one residue per bundles.

We consider that we have N_s analogous bundles, denoted $\mathcal{B}_1, \ldots, \mathcal{B}_{N_s}$, extracted from the rigidly co-registered images of N_s subjects. Our goal is to find the anatomical invariants in this collection of anatomical shapes as well as the description and the measure of their variability in the population. For this purpose, we will take advantage of the registration criterion introduced in the previous section to decompose the anatomical variability into a geo-

metrical part encoded in the diffeomorphisms and a "texture" part encoded in the residuals.

Following Allassonnière et al. (2007); Durrleman et al. (2009b), we consider that the bundles result from the deformations of an unknown template (i.e. a prototype bundle) plus residual perturbations in the space of currents. Formally, we can write that the observed bundles are instances of the following random process:

$$B_i = \phi_{i*}\overline{B} + \varepsilon_i \tag{10}$$

where the bundles B_i are seen as currents, ϕ_i are diffeomorphisms which deform the unknown template $\overline{B}$ (supposed to be a current as well) and ε_i are the residual perturbations which account for everything that cannot be captured by a regular deformation. The estimation of the template $\overline{B}$ will capture the anatomical invariants in the population. The estimation of the law (restricted here to the mean and the covariance) of the deformations and the residual perturbations will provide a quantitative description of the geometric and "texture" variability.

It has been shown in Durrleman (2010, Chap. 5) that we can define random Gaussian variables ε_i in the space of currents and random Gaussian diffeomorphisms (defined by random Gaussian variations of their tangent-space representation) such that the Maximum A Posteriori (MAP) estimation of the template, the deformations and the residuals is given by the minimization of the criterion:

$$\min_{\overline{B},\phi_i} \left\{ \sum_{i=1}^{N_s} \left\| \phi_{i*}\overline{B} - B_i \right\|_{W^*}^2 + \gamma \mathrm{Reg}(\phi_i) \right\} \tag{11}$$

The result of this minimization problem is an template $\overline{B}$, N_s diffeomorphisms ϕ_i and N_s residual currents $\varepsilon_i = B_i - \phi_{i*}\overline{B}$.

To optimize the criterion in Eq. (11), we use an alternative minimization procedure. We initialize the optimization with no deformation (i.e. $\phi_i(x) = x$). In this case, the template consists in the empirical mean of the bundles: $\overline{B} = \sum_{i=1}^{N_s} \mathcal{B}_i / N_s$, namely the union of every momenta of all bundles scaled by $1/N_s$ represented as a sum of Dirac delta currents. If the template is fixed, the minimization of the criterion leads to the parallel minimization of N_s criteria of the form of Eq. (9). Since the template is given as a finite sum of Dirac delta currents, these minimizations can be performed by registering the template to every bundle as explained in Sec. 3. If the deformations

are fixed, the current template is updated by minimizing the first term in Eq. (11) (the second one being constant): $\sum_{i=1}^{N_s} \left\| \phi_{i*}\overline{B} - \mathcal{B}_i \right\|^2_{W^*}$. This convex function is minimized in the space of currents by a gradient descent scheme. For the reasons explained in Durrleman et al. (2009b), the updated template results from the application of the sparse approximation method explained in Section 2.4. This has two consequences: first the template always remains a sum of Dirac delta currents during the iterations and, second, the estimated template has an 'optimal' number of momenta given the spatial scale of currents λ_W. Therefore, it compares to the approximated fiber bundles like the ones shown in Fig. 5 or 6.

4.2. Statistical analysis of deformations and residual perturbations

The minimization of the MAP criterion in Eq. (11) leads to the estimation of:

- 1 template $\overline{B}$ given as cloud of $N_{\overline{B}}$ oriented points $\overline{B} = \sum_{k=1}^{N_{\overline{B}}} \delta_{x_k}^{\tau_k}$,
- N_s deformations ϕ_i characterized by the initial momenta $(x_k, \alpha_k^i)_{k=1,\dots,N_{\overline{B}}}$ all located at the template points x_k,
- N_s residual currents: $\varepsilon_i = \mathcal{B}_i - \phi_{i*}\overline{B}$.

The residuals currents consist of the union of the momenta of $\mathcal{B}_i$ and those of $-\phi_{i*}\overline{B}$. Contrary to the momenta of deformations, the number and location of these current momenta are different for every subject. Nevertheless, we can project these currents into the same basis by projecting the momenta at the nodes of a regular lattice (see Durrleman (2010, Chap. 2) for details), where the projection error tends to zero when the step of the grid tends to zero. As a consequence, we can consider the residual currents as a feature vector decomposed in the same basis for every subject: they are all of dimension N_{grid}, the number of grid nodes. In practice, we will see in the sequel that we do not need to explicitly compute this projection on the grid.

To analyze the geometrical variability, we perform a Principal Component Analysis (PCA) on the feature vectors of deformations $(\alpha_k^i)_{k=1,\dots,N_{\overline{B}}}$ (of dimension $3N_{\overline{B}}$) with respect to the Sobolev metric induced by the kernel of the deformations[2] K^V. In practice, we build the $3N_{\overline{B}}$-by-N_s matrix of the

[2]so that the norm of a feature vector (α_k^i) is equal to the norm of the speed vector field $v(x) = \sum_k K^V(x, x_k)\alpha_k^i$ in the RKHS V, where x_k denotes the template points.

centered observations $A = (\alpha^1 - \overline{\alpha}, \ldots, \alpha^{N_s} - \overline{\alpha})$ (where $\overline{\alpha}$ is the sample mean vector $\sum_{i=1}^{N_s} \alpha^i / N_s$) and the $3N_{\overline{B}}$-by-$3N_{\overline{B}}$ block matrix $\mathbf{K}^V$ whose block (i,j) is the 3-by-3 matrix $K^V(x_i, x_j)$ ($\mathbf{K}^V$ is symmetric, definite positive by definition of the kernel K^V). Then, the sample covariance matrix of the initial momenta is given as: $\Sigma_V = (\mathbf{K}^V)^{1/2} A \left((\mathbf{K}^V)^{1/2} A \right)^t$, whose eigenvectors and eigenvalues are denoted α_m and λ_m^2 respectively. The eigenvectors parameterize the initial speed vector field of a deformation. A geodesic shooting enables to compute this deformation ϕ^m, called the mth mode of deformation at +1 standard deviation if one shoots the vector $\overline{\alpha} + \lambda_m \alpha_m$ and at -1 standard deviation if one shoots the vector $\overline{\alpha} - \lambda_m \alpha_m$.

To analyze the "texture" variability, we perform a PCA on the feature vector of residual currents provided by the Sobolev norm induced by the kernel K^W. The mean residue is the sample mean current $\overline{\varepsilon} = \sum_{i=1}^{N_s} \varepsilon_i / N_s$ of size $3N_{\text{grid}}$. The $3N_{\text{grid}}$-byN_s matrix of centered observations is given by: $\varepsilon = (\varepsilon_1 - \overline{\varepsilon}, \ldots, \varepsilon_{N_s} - \overline{\varepsilon})$. The metric is given by the N_{grid}-by-N_{grid} block-matrix $\mathbf{K}^W = (K^W(x_i^g, x_j^g))_{i,j}$ where the x_i^g's denote the grid nodes. The sample covariance matrix is given by: $\Sigma_W = \mathbf{K}^{W\,1/2} \varepsilon (\mathbf{K}^{W\,1/2} \varepsilon)^t$.

A usual trick when the number of subjects N_s is much smaller than the dimension of the observations N_{grid} is to find the eigenmodes of the N_s-by-N_s matrix $\Sigma'_W = \varepsilon^t \mathbf{K}^W \varepsilon$, which shares the same non-zero eigenvalues as Σ_W. The matrix Σ'_W is very easy to compute since its $(i,j)th$ term is given by $\langle \varepsilon_i - \overline{\varepsilon}, \varepsilon_j - \overline{\varepsilon} \rangle_{W^*}$ which can be computed using Eq. (7) and does not require to explicitly compute the grid projection. If E is the N_s-dimensional eigenvector of Σ'_W, then the corresponding eigenmode of Σ_W is given as[3]:

$$\varepsilon_m = \overline{\varepsilon} + \sum_{i=1}^{N_s} E_i (\varepsilon_i - \overline{\varepsilon})$$

As a consequence, this mth "texture" mode can be written as a weighted sum of the residual currents ε_i and hence a weighted sum of all the momenta of the input bundles $\mathcal{B}_k$ and the momenta of $-\phi_*^i \overline{\mathcal{B}}$ (i.e. $(\phi^i(x_k), -d_{x_k}\phi^i \tau_k)$). This highly redundant representation at the scale λ_W is approximated using the sparse approximation scheme explained in Section 2.4. This gives a much

[3]As explained in Durrleman (2010, Chap. 5), the norm of the mode equals the corresponding eigenvalue, so that there is no need to scale the mode by λ_m as it was done for the modes of deformation written as $\overline{\alpha} \pm \lambda_m \alpha_m$.

more interpretable representation of the m*th* texture mode, which locally integrates the positive and negative weights, as illustrated in Fig. 7.

4.3. Synthesis of new bundles

Our statistical estimations rely on a *generative* model: one fits a particular model to the observations. This means that the estimated variability can be used to simulate new synthetic fiber bundles which compares to the observations. This is helpful to better understand and interpret the anatomical variability captured by the model. The simulation follows the generative model given in Eq. (11): one simulates a deformation ϕ and a residue ε and build the simulated bundle: $\phi_* \overline{B} + \varepsilon$.

To simulate realistic bundle, one needs to take into account the correlations between the modes of deformations and the modes of the residuals. For this purpose, we build a concatenated feature vector of dimension $N_{\overline{B}} + N_{\text{grid}}$: $(\alpha^i, \varepsilon^i)$ for each subject. Once these feature vectors have been centered, we build the N_s-by-N_s sample covariance matrix $\Sigma'_{V \otimes W}$ whose term (i, j) is given by: $\frac{\langle \alpha^i, \alpha^j \rangle_V}{\sigma_\alpha^2} + \frac{\langle \varepsilon^i, \varepsilon^j \rangle_{W^*}}{\sigma_\varepsilon^2}$, where the inner-product in the RKHS V is given by $\langle \alpha^i, \alpha^j \rangle_V = \alpha^i \mathbf{K}^V \alpha^j = \sum_{p,q} (\alpha_p^i)^t K^V(x_p, x_q) \alpha_q^j$, σ_α^2 is the variance of the initial momenta (trace of the matrix Σ_V normalized by $1/(N_s - 1)$) and σ_ε^2 the variance of the residuals (trace of the matrix Σ_W normalized by $1/(N_s - 1)$).

Let $V_1, \ldots, V_{N_{\text{modes}}}$ the N_{modes} first eigenmodes of the matrix $\Sigma'_{V \otimes W}$ (these vectors are of dimension N_s) and $\gamma_1, \ldots, \gamma_{N_{\text{modes}}}$ independent Gaussian variables with zero mean and unit variance. Then, one simulates initial momenta and residue thanks to a random superposition of the eigenmodes. Initial momenta are simulated according to:

$$\alpha = \overline{\alpha} + \sum_{m=1}^{N_{\text{modes}}} \gamma_m \sum_{k=1}^{N_s} V_{m,k} (\alpha^k - \overline{\alpha})$$

and a residue according to:

$$\varepsilon = \overline{\varepsilon} + \sum_{m=1}^{N_{\text{modes}}} \gamma_m \sum_{k=1}^{N_s} V_{m,k} (\varepsilon^k - \overline{\varepsilon}),$$

where the same weight γ_m are used for both α and ε (for that it is one single feature vector (α, ε)).

Finally, we shoot the initial momenta to give an instance of the deformation ϕ and build the simulated bundle as $\phi_* \overline{B} + \varepsilon$. This simulated bundle is

again a weighted sum of all the momenta in the database plus the momenta of the deformed bundle $\phi_* \overline{B}$. The sparse approximation yields a representation of this simulated bundle which compares to the sparse approximation of the original bundles.

4.4. Parameters

The estimation of the template, deformations and residual perturbations as well as the subsequent statistical analysis of variability depends on 4 parameters whose impact on the results may be easily understood:

- the size of the deformation kernel λ_V, which determines the typical distance under which the points move in a correlated manner, thus controling the 'rigidity' of the diffeomorphisms,
- the size of the kernel of currents λ_W, which determines the spatial "resolution" at which one considers the fiber bundles,
- the trade-off between regularity and fidelity-to-data γ,
- the sparsity parameter ρ, which determines the accuracy of the sparse approximation. The smaller, the better the approximation, the higher the number of estimated momenta.

The sparsity parameter ρ is usually fixed to 5% of the variance, as a good balance between approximation error and sparsity (see Durrleman (2010, Chap. 3) for more discussion about this parameter). The three other parameters λ_V, λ_W and γ controls where to put the boundary between the geometrical variability and the "texture" variability. In the actual stage of development of the methodology, these parameters are manually set by considering the scale of the anatomical features one wants to detect to set the scale of current λ_W, the scale at which these features vary to set the scale of deformation λ_V and the accuracy of pair-wise registration to set the trade-off γ. These parameters are then adjusted by looking at the results of registration between pairs of data. The next step would be to integrate the estimation of these parameters along with the estimation of the template and deformations by analogy with what is done in Allassonnière et al. (2008) for instance.

5. Experimental results

Six brain DTI data sets acquired on a 1.5T GE scanner on healthy volunteers were used in this study. Image dimensions are $128 \times 128 \times 30$, and resolution is $1.8 \times 1.8 \times 4$mm. 25 non-collinear diffusion gradients and a b-value of $1000 s/mm^2$ were used. Fiber tractography was performed using MedINRIA[4], which includes a robust tensor estimation and a streamline tractography algorithm using log-Euclidean tensor interpolation (Fillard et al., 2007a). Manual segmentation of five fiber bundles was done: the entire corpus callosum, the corticospinal and the corticobulbar tracts, and the left and right arcuate fasciculi (Fig. 12-a).

Fibers within a bundle and across the subjects need to be oriented in a consistent manner. The tractography algorithm we used does not necessarily provide consistently oriented fibers. To orient them, we use a simple empirical procedure. First, we pick a fiber among the longest one, which is representative of the geometry of the tract, and define the orientation of the bundle as the orientation of the vector connecting their two extremities. Then, we orient the fibers so that the vector connecting the two extremities of each fiber has a positive inner-product with the pre-defined orientation. This procedure correctly orients most fibers, except those, which have a transversal orientation (typically small fibers within a bundle with a 'U' shape, for instance). We manually correct the orientation of those fibers.

In Section 5.1, we evaluate the registration method explained in Section 3 by registering the bundles of two subjects and comparing the result with FA and tensor registration. In Section 5.2, our framework for atlas construction explained in Section 4.1 is evaluated with the construction of a diffeomorphic atlas of the five bundles of our data set. The statistical analysis of the corticobulbar and cortico-spinal tract is performed as explained in Section 4.2. In Section 5.3, we illustrate the variability captured by the model by simulating new synthetic bundles as explained in Section 4.3.

5.1. Fiber Bundle Registration

In this section, we performed registration between the sets of 5 fiber bundles of two different subjects. The alignement of fiber bundles is compared with the one obtained from the registration of the images of Fractional Anisotropy (FA) using the method of Vercauteren et al. (2007) and from the

[4]http://www-sop.inria.fr/asclepios/software/MedINRIA/

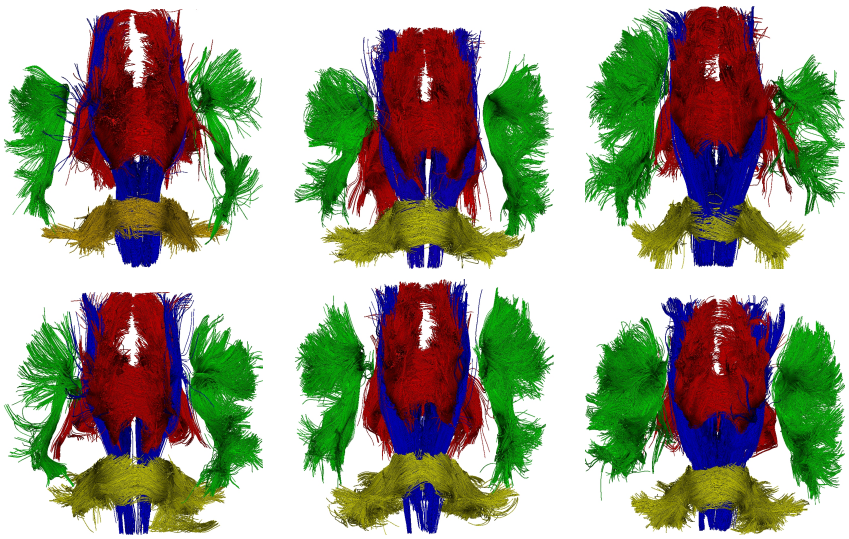

Figure 8: Five fiber bundles extracted in six subjects using MedINRIA. **Blue:** the corticospinal tract. **Yellow:** the corticobulbar tract. **Red:** the callosal fibers. **Green:** the left and right arcuate fasciculi.

registration of the images of tensors using the method of Yeo et al. (2009). For FA and tensor-based registration, deformation fields were computed between images and applied to bundles afterwards: bundles were not tracked again after registration. The three methods produce diffeomorphic transformations and can be compared. The parameters were adjusted to produce deformations of about the same smoothness. Concerning our registration scheme, we set the regularity of the deformation $\lambda_V = 20$mm, the spatial scale of the currents $\lambda_W = 5$mm and the trade-off between regularity and fidelity-to-data: $\gamma = 10^{-4}$. For clarity purposes, we present registration results of two bundles only: the corpus callosum (CC) (Fig. 9) and the corticospinal tract (CST) (Fig. 10), since they highlight the most striking differences between methods, although the 5 fiber bundles have been taken into account during registration.

Fig. 9a shows two misaligned corpus callosa. Fig. 9b,c presents the registration of those bundles computed using respectively FA and tensor images. The registration of the fiber bundles with our method (Fig. 9d) shows a greater overlap, synonym of a better alignment. Local improvements are noticeable in the left and right parts of the genu. This result shows that the

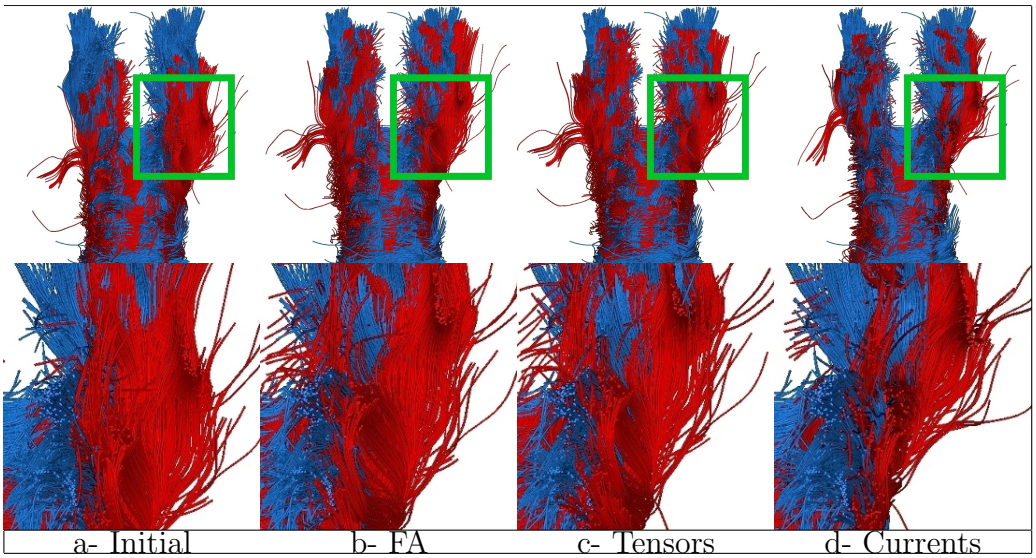

Figure 9: Diffeomorphic registration of two corpus callosum fibers. Bottom images are a close-up on the green squared region. Initial tracts (a) and registered tracts using FA (b), tensors (c) or fiber bundles (d) as constraints. Overlap of blue and red fiber bundles is greater using currents, especially in the left and right parts of the genu of the corpus callosum.

anatomical information contained in the extracted fiber bundles acts as a stronger prior than the tensor images to align the fiber bundles. Moreover, one can still notice few red fibers not aligned with the blue bundle in the exterior of the tract, which illustrates the robustness of our methodology to outliers. Indeed, these few fibers have a little weight in the dissimilarity measure in Eq. (9) compared to the rest of the bundle.

Registration of two cortico-spinal tracts shows similar effects, especially in the anterior part expanded in a green square in Fig. 10. In those regions, multiple bundles may coexist whereas FA and tensor images are uniform, as illustrated in Fig. 11. For image-based registration, this region is a uniform tensor field or a region of uniform FA intensity. In absence of image gradient, there is no reason that an iconic registration retrieves any deformation in such regions. By contrast, the fiber bundle registration is constrained by the boundary between two different bundles. The fiber bundle registration is constrained by macroscopic structures, whereas image registration is constrained by local gradients of the diffusivity properties. In a general manner, fiber bundles registration is based on a selection of some information in the

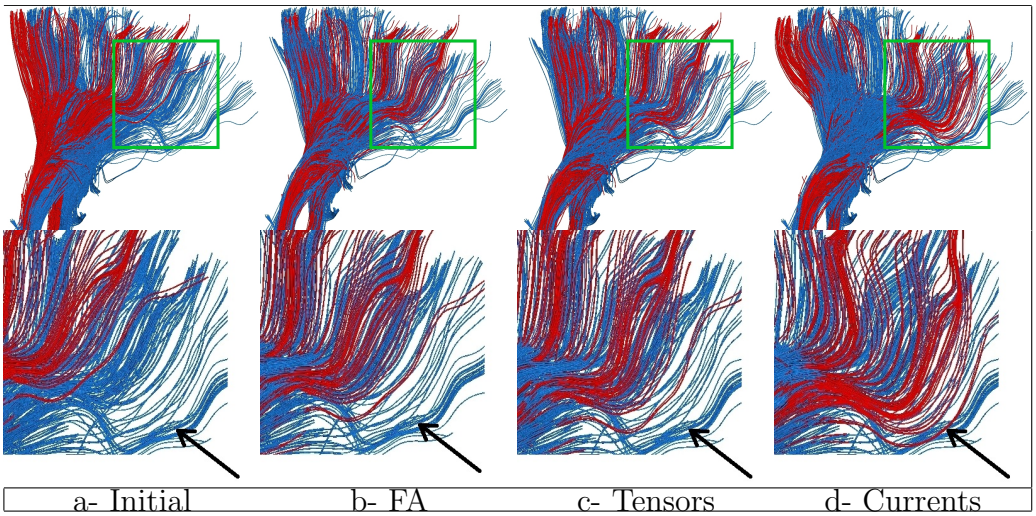

Figure 10: Registration of two corticospinal tracts. Bottom images are a close-up on the green squared region. Initial tracts (a) and registered tract using FA (b), tensors (c) or fiber bundles (d) as constraints. Currents better warp the red fibers in the anterior part of the tract. FA and tensor-based approaches do not well align fiber bundles, since the image gradient vanishes in this region. Registration in the posterior part is mainly constrained by the corpus callosum which strongly pushes the fibers toward the posterior part of the brain.

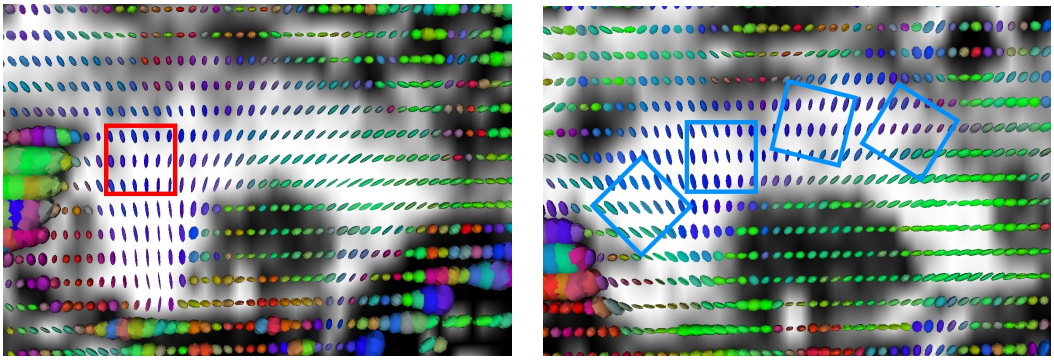

Figure 11: Effect of the clustering for registration. Two tensor fields overlapped with FA images are shown (sagittal slice, around the corona radiata). Without any prior, it is impossible to determine whether the red square on the left image matches with any of the blue square on the right image, since the tensor field is uniform in this region. By contrast, clustering fibers into anatomical bundles introduces boundaries which are invisible in the original images and which are taken into account as constraints in our registration scheme.

images and on an addition of anatomical information which are not contained in the images. For instance, at fiber crossings, the fiber bundle registration is constrained by two distinct bundles, whereas the two selected directions are integrated into a single tensor (or single orientation distribution function) in images. One has selected two directions in the orientation distribution function on the basis of anatomical considerations (the current knowledge of fiber bundle organization) which are not contained in the images, thus breaking the isotropy of the tensor. Similarly, the clustering of the fibers into bundles accounts for the anatomical knowledge of the expert in case of manual clustering, or for some anatomical priors in case of automatic clustering. For this reasons, we think that the fiber bundle registration is based on more realistic anatomical assumptions than image registration.

We notice also in Fig. 10, that the posterior parts of the cortico-spinal tracts seems not to be properly aligned. This is due to the presence of the corpus callosum in this region which strongly pushes the fibers toward the posterior part of the brain. We recall that the registration consistently integrates the different spatial constraints, which might be contradictory, into a single deformation of the white matter. Here, the corpus callosum has much more fibers than the cortico-spinal tract and therefore has a stronger weight in the matching criterion than the corticospinal tract, thus acting as a stronger constraint. The method can achieve a different compromise by adjusting the weight of the different fiber tracts in the matching criterion according to the confidence one has in its extraction and selection. However, how to determine such weights on an anatomical basis still remains an open question.

5.2. Construction of atlas of fiber bundles

As explained in Section 4, we estimate a template such that the input dataset results from random deformations of this template plus random perturbations in the space of currents. For each subject, there are one single deformation and 5 independent perturbations. The template consists of the five prototype bundles shown in Fig. 12. It has been computed by fixing the spatial scale of currents to $\lambda_W = 5$mm, of deformations to $\lambda_V = 20$mm and the trade-off between regularity and fidelity-to-data to $\gamma = 10^{-4}$.

The template captures the anatomical invariants across the subjects in the sense of the generative model in Eq. (10). As explained in Section 4.1, its estimation requires the use of the sparse approximation. Therefore, the template has an 'optimal' number of momenta at the scale of analysis λ_W

and compares to the approximated original bundles shown in Fig. 6 or 16b for instance.

The template could be used in combination with atlas-to-subject registration to automatically gather fibers of a given subject into fiber bundles and to associate anatomical labels to these fiber bundles. Indeed, one could consider the whole set of extracted fibers as a single current and apply the registration between the template and the subject's whole set of fibers. Then, closest fibers strategies could be use to associate a label to every fiber.

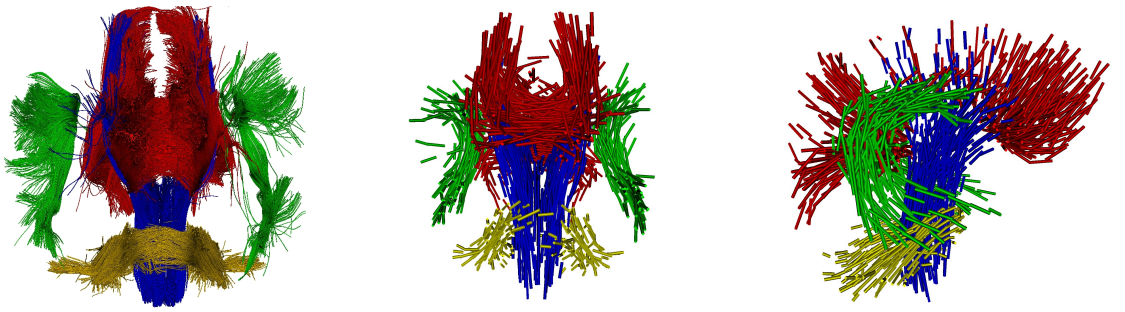

(a) One subject (b) template (occipital view) (c) template (lateral view)

Figure 12: **Template of five bundles**: the corticospinal tract (blue), the corticobulbar tract (yellow), the callosal fibers (red), the left and right arcuate fasciculi (green). (a): one subject among the six of the data set. (b,c) the atlas estimated such that original data result from random deformations of the template plus random perturbations.

5.3. Statistical analysis of the variability

In this section, we focus on each bundle separately. This means that we re-estimate an atlas (template, deformations and residual perturbations) separately for each bundle. All the experiments described here used the same set of parameters: size of deformation kernel $\lambda_V = 20$mm, size of current kernel $\lambda_W = 5$mm, trade-off regularity/fidelity-to-data $\gamma = 10^{-4}$ and sparsity parameter $\rho = 5\%$.

Note that we could have used the residuals of the atlas estimated in the previous section to describe the possible correlations between different bundles. For the sake of simplicity, we focus here on the single bundle case to highlight the strengths of the method. We leave for future work the application of the method in the multi-bundle case. The quantitative analysis of the correlations between the modes of variability of different bundles can

be done straightforwardly in this framework. However, the question of its illustration and its interpretation has still to be addressed.

5.3.1. Variability of the cortico-bulbar tract

We focus now on the analysis of the corticobulbar tract which is described by both the modes of deformation (geometrical variability) and the modes of residual perturbation ("texture" variability). The geometrical variability is measured by the initial momenta of the template-to-subjects deformations. As a result of the MAP estimation of the template, these momenta appears to be centered: the norm of the mean momenta is 0.42 times the standard deviation ($\|\overline{\alpha}\|_V = 0.42\sigma_\alpha$ with the notation of Section 4.2), which is not significantly different from 0: for the 6 subjects, the t-statistics is equal to $\sqrt{6} * 0.42 = 1.03$ with a p-value greater than 0.3. The first mode of the deformations at $\pm\sigma$ (resulting from the geodesic shooting of the first mode of the initial momenta) is shown in Fig. 13a. The main variations are a torque of the frontal part of the bundle, as well as a stretching/shrinking of its lateral parts. Further investigation should determine whether this torque is related to the well-known brain torque.

The variability in terms of "texture" is captured by the residual currents. The residuals are centered: the mean current is 0.36 times its standard deviation ($\|\overline{\varepsilon}\|_W = 0.36\sigma_\varepsilon$ with the notation of Section 4.2) which leads to a p-value greater than 0.31. The first residual mode m_ε is shown in Fig. 13-b. It shows an asymmetry in the number of fibers in each lateral part of the bundle. This result shows, undoubtedly, that the variability left aside from the diffeomorphisms is not just noise, *but still contains some interesting anatomical features*. This shows the interest of our modeling which takes into account all the available geometrical information without imposing strong priors on the kind of variations we are looking for.

5.3.2. Variability of the cortico-spinal tract

Here, we focus on the variability analysis of the cortico-spinal tract. The estimated template is shown in the middle panels in Fig 14 and Fig. 15.

The norm of the mean initial momenta is $\|\overline{\alpha}\|_V = 9.87$mm and its standard deviation is $\sigma_\alpha = 21.7$mm (with the notations of Section 4.2). The ratio mean to standard deviation ratio is therefore of 0.45 which gives p-value greater than 0.36. The two first modes of the deformations are shown in Fig 14. These modes mainly show variations of the shape of the stem of the bundle and an left/right asymmetry.

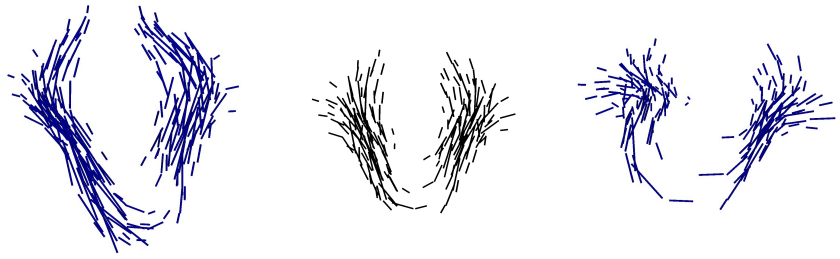

def. mode at $-\sigma$ template def. mode at $+\sigma$

a- **First mode of deformation at $\pm\sigma$**

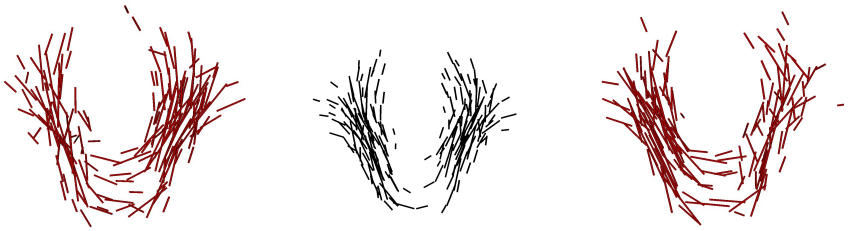

texture mode at $-\sigma$ template texture mode at $+\sigma$

b- **First "texture" mode at $\pm\sigma$**

Figure 13: First mode of geometry and texture for the cortico-bulbar tract (axial view). **Top: First mode of deformation**: the diffeomorphic variability of the population around the prototype bundle (middle) is mainly a torque at the basis of the bundle and a stretching/shrinking effect of the left and right parts of the bundle. **Bottom: First texture mode**: This mode captures the residual variability of the population, once the diffeomorphic variability has been discounted. This mode is added to (right) or removed from (left) the prototype bundle (middle). The mode at $+\sigma$ (resp. $-\sigma$) shows that the left (resp. right) part of the bundle becomes thicker, while its right (resp. left) part becomes thiner. It shows an asymmetry in terms of density of fibers between the two branches of the tract.

The norm of the mean residue is $\|\overline{\varepsilon}\|_{W^*} = 610$mm and its standard deviation is $\sigma_\varepsilon = 1751$mm (with the notations of Section 4.2). The mean to standard deviation ratio is therefore of 0.35, which leads to a p-value greater than 0.3. The first mode of the residuals is shown in Fig. 15. It shows a global variation of the fiber density across subjects. This variation of density seems to occur in the whole bundle, contrary to the first texture mode of the corticobulbar tract (in Fig. 13) which shows an asymmetry of the fiber density within the bundle.

5.3.3. Synthesis of new bundles

As explained in Section 4.3, one can analyze the correlations between the modes of deformations and the mode of "texture" and then use this estimated variability to simulate new bundles. Several instances of such simulated bundles are shown in Fig. 16c. For this simulation, we use the $N_{\text{modes}} = 4$ first modes of variations (among the $N = 6 - 1 = 5$ possible for centered PCA), which represents 94% of the estimated variability. The last mode, which corresponds to the smallest eigenvalue representing only 6% of the variability, is likely to encode only noise. The simulated bundles, which also results from the application of the sparse approximation, compare to the approximated original bundles shown in Fig. 16b.

This simulation illustrates the variability which has been captured by the deformations and the residual perturbations. It shows realistic bundles with various shapes and various fiber densities. Comparing the simulated bundles with the original ones enables to better understand and interpret the reproducible features which have been detected consistently across the subjects. Of course, the small number of subjects used in this study limits the relevance of the conclusions that one may draw from this experiment. Nevertheless, it shows how this method can be used routinely to analyze, measure and interpret the anatomical variability of white matter bundles. Using a much larger database should lead to a better understanding of the normal and the pathological variability of these anatomical structures.

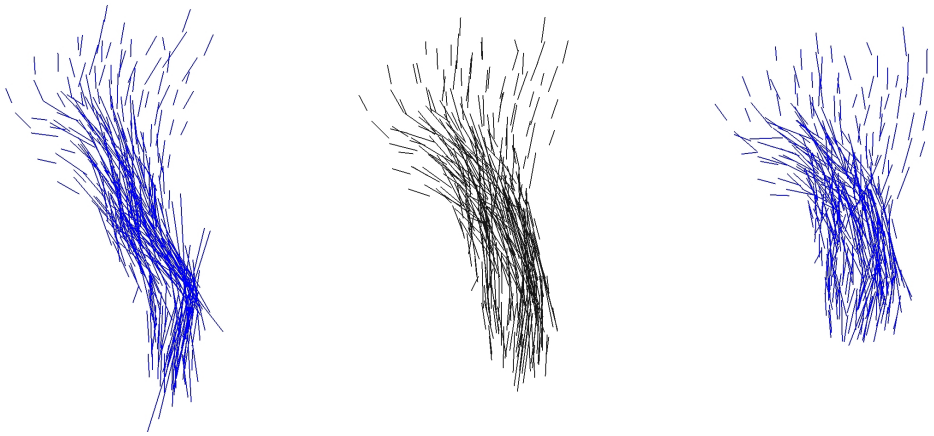

a- **1st mode of deformation** of the cortico-spinal tract (lateral view)

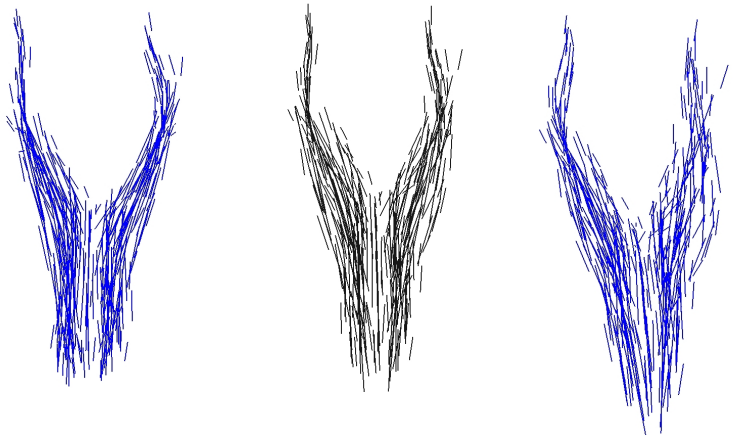

b- **2nd mode of deformation** of the cortico-spinal tract (frontal view)

Figure 14: First and second mode of deformation at $\pm\sigma$ of the corticospinal tract. The first mode shows an elongation/shrinkage effect of the stem of the bundle with a torsion effect and a widening effect of the superior part of the bundle. The second mode shows an asymmetry of the position of the two branches with respect to the spinal cord.

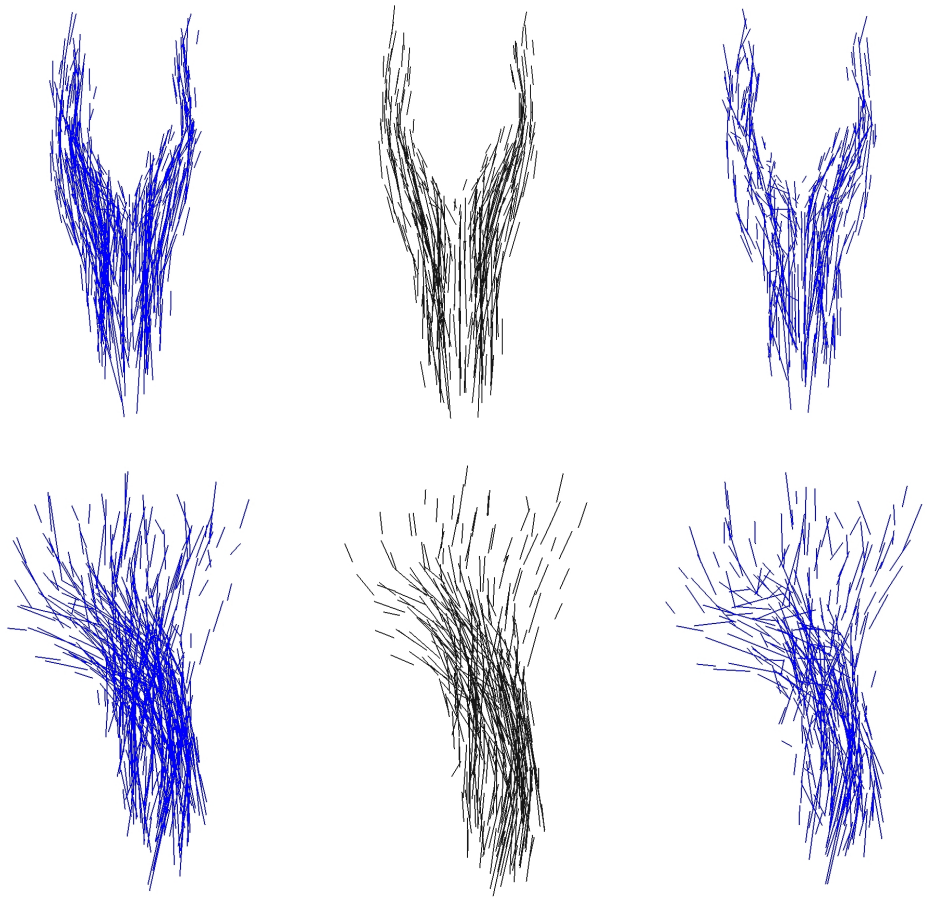

Figure 15: **First texture mode** of the cortico-spinal tract. This mode shows first a variability in terms of fiber density (visible on the frontal view - top row) and a variability of the width of the superior part of the bundle (visible in the lateral view - bottom row).

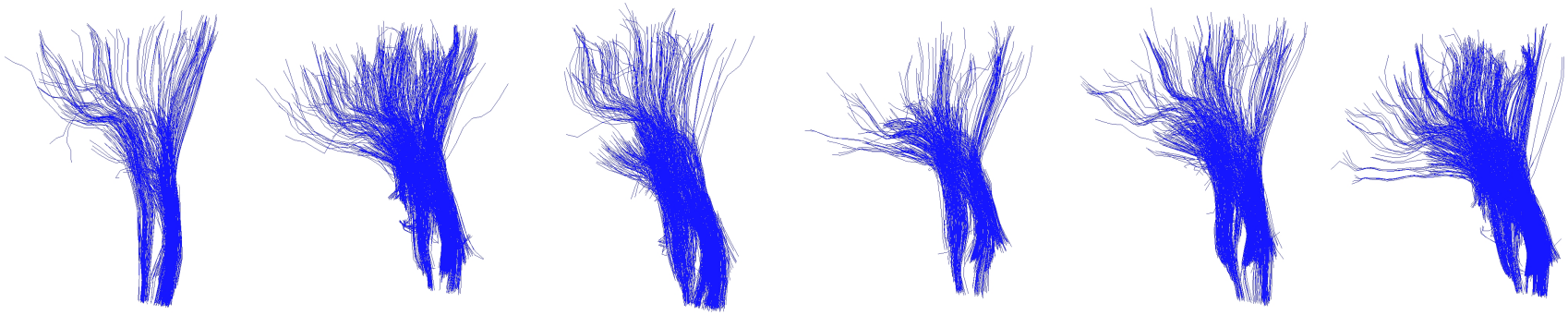

a- Original fiber bundles (cortico-spinal tract, lateral view)

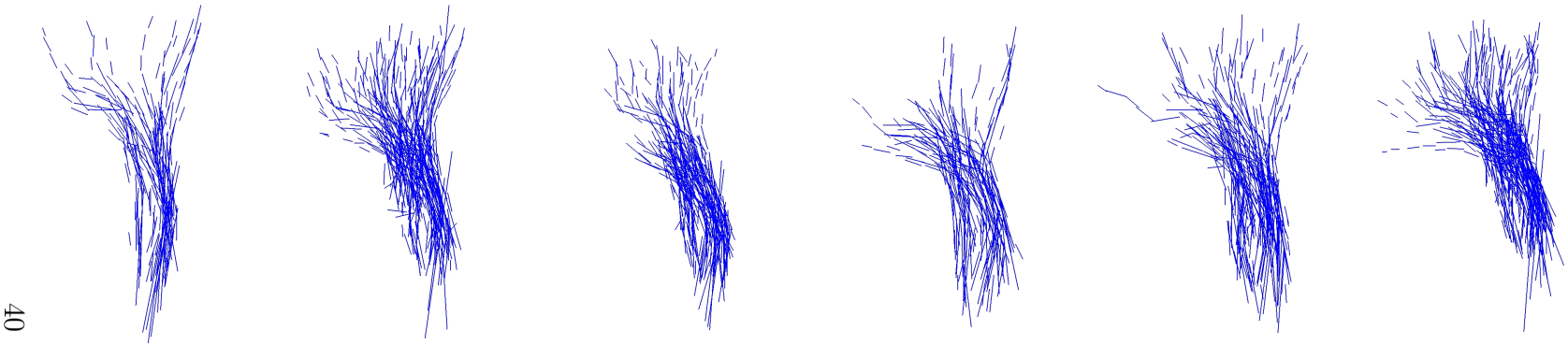

b- Approximated fiber bundles with $\lambda_W = 5$mm

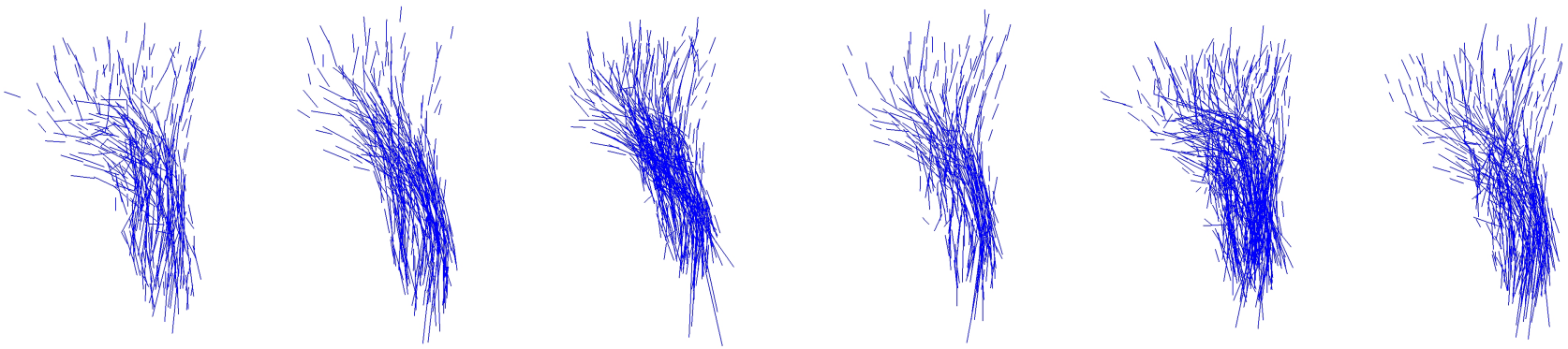

c- Six instances of bundles simulated according to the variability estimated from the original population
$\lambda_W = 5$mm, $\lambda_V = 20$mm and $\gamma = 10^{-4}$

Figure 16: Our statistical model is generative, thus allowing to simulate new bundles by combining the estimated geometrical and "texture" variability (c). These simulated bundles compare to the approximation of the original ones shown in b. This comparison helps to better understand and interpret the reproducible features which have been detected consistently across the original data (a). In this simulation, the first 4 modes of variability were used, which represents 94% of the total variability. The simulated bundles reproduce well the various shapes and fiber densities that one finds in the original data at the spatial resolution $\lambda_W = 5$mm.

6. Discussion and conclusion

In this paper, we proposed a novel framework for the statistical analysis of fiber bundles using currents. The metric on currents does not impose either point-to-point or fiber-to-fiber correspondences, a crucial feature in regards to the variability of tractography algorithms outputs. It is also robust to outliers and weakly dependent of the sampling of the fibers. It enables to measure the differences between fiber bundles both in terms of their geometry (boundaries, fiber distribution, etc..) and in terms of "texture", which includes in particular, the density of fibers.

This metric has been used to drive the registration between sets of homologous fiber bundles. Fiber bundles are seen as anatomical landmarks which constrain the estimation of the deformation of the underlying white matter. Comparisons with the alignment obtained from the registration of images of Fractional Anisotropy or images of tensors highlight the different methodological approaches. In particular, iconic registration is less adapted to align fiber bundles, since this registration is not directly constrained by the fiber bundles themselves, but indirectly by the change of diffusivity that these fibers induce. Moreover, the smoothness constraint which is imposed during fiber extraction adds realistic anatomical priors for the registration, which are not taken into account during iconic registrations. The clustering of fibers into bundles introduces boundaries, which are not visible in images, especially in area where the tensor field is homogeneous and at fiber crossings where two fiber bundles may coexist, whereas their diffusivity properties are integrated into a single tensor in the images. In the future, the registration will be also assessed the other way round, namely by using the fiber-bundle registration to align images and compare the results with iconic registration. It is likely that the fiber-bundle registration correctly align intensities in region close to the tracts, whereas the image alignment will suffer from the lack of information in regions far from the extracted bundles, as this has been already noticed in the context of lung imaging (Gorbunova et al., 2010).

The metric on currents and the derived registration have been used then in a statistical context. A generative model of variability of fiber bundle is introduced: homologous fiber bundles are seen as random deformations of an unknown template plus random perturbations. The template estimates the invariant features across a population. In the future, it could be used in combination with registration to extract and label fiber bundles in new subjects. The estimated laws of the deformations and of the residual pertur-

bations provide a measure of the geometric and "texture" variabilities. Our experiments show consistent results with known anatomical variability like the brain torque for the corticobulbar tract, which is put in evidence for the first time on fibers. Even with such a small dataset, our analysis managed to decompose the variability into two parts that are likely to describe relevant anatomical features. Of course, the anatomical findings should be strengthen by using larger dataset in the future. In this respect, automatic bundling can be used to produce a complete set of anatomically relevant fiber bundles, as in El Kouby et al. (2005); Maddah et al. (2007). We need also to set up a more automatic procedure to consistently orient the fibers within a bundle and across subjects, to limit the user intervention. For instance, we can adapt the tractography algorithm so that they provide fibers with consistent orientation. This should be possible in case of streamline tractography algorithm based on a selection of seed points. Another solution would be to adapt the framework of currents, so that it becomes blind to the orientation of the fibers. For instance, one could investigate the idea of representing a non-oriented curve by a collection of tensors of the type $\tau\tau^t$, where τ is the tangent of the curve.

Our method does not only gives statistical measures of variability, but it also illustrates the variability in an interpretable way. The key tool used in this framework to produce interpretable illustrations is the sparse approximation of currents. The modes of deformation, the modes of texture and the simulation of new data according to the estimated variability show in an interpretable way what is the variability captured by the model. It helps to understand which features the model detects consistently across the subjects. Such an analysis should lead to anatomical findings like the characterization of pathologies affecting brain connectivity. This differs from purely descriptive statistical measures, like hypotheses testing on set of feature vectors for group separation, which does not explain what makes the populations different.

The interpretation of the variability should be used, at first, to investigate the bias introduced by the priors of the tractography and fiber selection and eventually to better distinguish the variability which comes from processing artifacts from the true underlying anatomical variability. For instance, the variations in terms of fiber density may be caused by the tractography algorithm itself, as fiber density is generally an arbitrary parameter set by the method. Some methods initiate fibers at the center of every voxels, some others over-sample voxels to produce more fibers. In this respect, the global

variations of fiber density in the cortico-spinal tract retrieved in the first texture mode may come from a bad control of the fiber density during fiber extration and clustering. By contrast, the asymmetry of fiber density between the right and left branch of the corticobulbar tract is more likely to be related to a true anatomical variability, for what the extraction and clustering methods are less likely to produce systematically asymmetric results. A better control on the density of extracted fibers should help to remove (or at least to precisely estimate) the bias introduced by the tractography and clustering algorithms. One solution would consist in relating this density to physical properties of the neural fibers, like the neural flux transported by the bundle or such that the estimated fiber bundle could explain the measures of diffusion. In the framework of currents, one could also imagine to weight each oriented point to give more or less importance to some bundles or parts of bundles. For instance, FA could be used as attributes to relax the geometrical constraints in regions where the FA is low, namely where the tracking returns less reliable fibers.

Our atlas construction and statistical analysis is based on a generative model which does not make strong assumptions on the kind of variability one is looking for. The method accounts for all the available information and decompose it into two terms: geometry and "texture". The main assumption resides in the boundary between the two terms, which is determined by the values of three regularity parameters. These parameters have been set manually in our experiments, although an alternative approach would be to estimate these parameters along with the atlas in the framework of Bayesian mixed effects models as in Allassonnière & Kuhn (2009) for instance. By contrast, the variability model proposed in Corouge et al. (2006) relies on much stronger assumptions: the fibers within a bundle are seen as the random Gaussian deformations of a single "mean" fiber. This approach requires to find homologous points between fibers, which makes the framework not robust to fiber interruption for instance. The Gaussian assumptions also limits the possible shapes of the bundles: in each plane orthogonal to the mean fiber, the point distribution should look like a Gaussian distribution. Fiber bundles simulated according to this model would have all exactly the same fiber density profile: high density close to the mean curve which decreases in every direction like a Gaussian function as one moves away from the mean curve. Such a model does not realistically account for the various density profiles one may find in different bundles.

The proposed approach could be extended in several ways. First, the

framework easily allows to take into account various anatomical landmarks both in the white and the grey matter: gyri, sulci, cortical surface, fiber bundles, subcortical structures, etc. This opens up the possibility to better constrain the registration between the anatomy of two subjects with more anatomical information and to build an atlas which would combine all the available information in a consistent way. The presented statistical analysis considers the variability of each fiber bundle individually. However, the framework can be also used to study the correlations between the modes of variations of different bundles. This would lead to a model of variations of a whole set of homologous bundles. Moreover, we should investigate the correlations between the estimated anatomical variability and functional or physiological signals. In particular, the alignment of fiber bundles should be assessed with respect to their ability to normalize fMRI signals. Correlations between the anatomical variations of the fiber bundles and the activation of some functional areas would be worth being investigated.

Our method is based on a generative statistical model which assumes the texture variability to be described in the reference frame of the subjects. As discussed in Durrleman et al. (2008), this model seems better suited from a statistical and computational point of view than alternatives approaches like Glaunès & Joshi (2006) in which the texture variability is described in the reference frame of the template. The variability analysis of the fiber bundles could be used in the future as a good study case to investigate the comparison between both approaches more in depth.

In this work, we used diffeomorphic registration to capture geometric differences and analyze the residuals for non-geometric variations. In the future, we could investigate to extend the diffeomorphisms to more complex deformation processes which allow to change the density of the fibers along with the geometry of the fiber bundles, in the spirit of the metamorphosis proposed for images (Trouvé & Younes, 2005). Then, the geometric and "texture" variability would be combined into a single non-diffeomorphic deformation.

Acknowlegments. We would like to thank Denis Ducreux, MD, Bicêtre Hospital, Paris, for providing the brain datasets. We thank anonymous reviewers for their insightful comments. This work was partially supported by European IP project Health-e-child (IST-2004-027749) and Microsoft Research.

References

Alexander, D. C., Pierpaoli, C., Basser, P. J., & Gee, J. C. (2001). Spatial transformations of diffusion tensor magnetic resonance images. *Transactions on Medical Imaging*, *20*, 1131–1139.

Allassonnière, S., Amit, Y., & Trouvé, A. (2007). Towards a coherent statistical framework for dense deformable template estimation. *Journal of the Royal Statistical Society Series B*, *69*, 3–29.

Allassonnière, S., & Kuhn, E. (2009). Stochastic algorithm for bayesian mixture effect template estimation. *ESAIM Probability and Statistics*, . In Press.

Allassonnière, S., Kuhn, E., & Trouvé, A. (2008). Construction of Bayesian deformable models via a stochastic approximation algorithm: A convergence study. *Bernoulli Journal*, . In press.

Aronszajn, N. (1950). Theory of reproducing kernels. *Transactions of the American Mathematical Society*, (pp. 337–404).

Basser, P. J., Pajevic, S., Pierpaoli, C., Duda, J., & Aldroubi, A. (2000). In vivo fiber tractography using DT-MRI data. *Magnetic Resonance in Medicine*, *44*, 625–632.

Batchelor, P. G., Calamante, F., Tournier, J.-D., Atkinson, D., Hill, D. L. G., & Connelly, A. (2006). Quantification of the shape of fiber tracts. *Magnetic Resonance in Medicine*, *55*, 894–903.

Besl, P., & McKay, N. (1992). A method for registration of 3d shapes. *IEEE Trans. on PAMI*, *14*, 239–256.

Cao, Y., Miller, M. I., Winslow, R. L., & Younes, L. (2005). Large deformation diffeomorphic metric mapping of vector fields. *Transactions on Medical Imaging*, *24*.

Chen, Y., & Medioni, G. (1991). Object modelling by registration of multiple range images. In *IEEE Proc. Conf. Rob. Auto.* (pp. 2724–2729).

Corouge, I., Fletcher, P., Joshi, S., Gouttard, S., & Gerig, G. (2006). Fiber tract-oriented statistics for quantitative diffusion tensor MRI analysis. *Medical Image Analysis*, (pp. 786–798).

Delmaire, C., Vidailhet, M., Wassermann, D., Descoteaux, M., Valabregue, R., Bourdain, F., Lenglet, C., Sangla, S., Terrier, A., Deriche, R., & Lehericy, S. (2009). Diffusion Abnormalities in the Primary Sensorimotor Pathways in Writer's Cramp. *Arch Neurol*, *66*, 502–508.

Descoteaux, M., Deriche, R., Knoesche, T., & Anwander, A. (2008). Deterministic and probabilistic tractography based on complex fiber orientation distributions. *Transactions in Medical Imaging*, .

Ding, Z., Gore, J. C., & Anderson, A. W. (2003). Classification and quantification of neuronal fiber pathways using diffusion tensor MRI. *Magnetic Resonance in Medicine*, *49*, 716–721.

Durrleman, S. (2010). *Statistical models of currents for measuring the variability of anatomical curves, surfaces and their evolution*. Thèse de sciences (phd thesis) Université de Nice-Sophia Antipolis.

Durrleman, S., Fillard, P., Pennec, X., Trouvé, A., & Ayache, N. (2009a). A statistical model of white matter fiber bundles based on currents. In J. L. Prince, D. L. Pham, & K. J. Myers (Eds.), *Proceedings of Information Processing in Medical Imaging (IPMI'09)* (pp. 114–125). Springer volume 5636 of *LNCS*.

Durrleman, S., Pennec, X., Trouvé, A., & Ayache, N. (2009b). Statistical models of sets of curves and surfaces based on currents. *Medical Image Analysis*, *13*, 793–808.

Durrleman, S., Pennec, X., Trouvé, A., Thompson, P., & Ayache, N. (2008). Inferring brain variability from diffeomorphic deformations of currents: an integrative approach. *Medical Image Analysis*, *12/5*, 626–637.

El Kouby, V., Cointepas, Y., Poupon, C., Rivière, D., Golestani, N., Pallier, C., Poline, J.-B., Bihan, D. L., & Mangin, J.-F. (2005). MR diffusion-based inference of a fiber bundle model from a population of subjects. In *Proc. of MICCAI* (pp. 196–204). Springer volume 3749 of *LNCS*.

Faria, A. V., Zhang, J., Oishi, K., Li, X., Jiang, H., Akhter, K., Hermoye, L., Lee, S.-K., Hoon, A., Stachinko, E., Miller, M. I., van Zijl, P. C., & Mori, S. (2010). Atlas-based analysis of neurodevelopment from infancy to adulthood using diffusion tensor imaging and applications for automated abnormality detection. *NeuroImage*, *In Press, Uncorrected Proof*, –.

Fillard, P., Arsigny, V., Pennec, X., & Ayache, N. (2007a). Clinical DT-MRI estimation, smoothing and fiber tracking with log-Euclidean metrics. *Transactions on Medical Imaging*, *26*, 1472–1482.

Fillard, P., Arsigny, V., Pennec, X., Hayashi, K., Thompson, P., & Ayache, N. (2007b). Measuring brain variability by extrapolating sparse tensor fields measured on sulcal lines. *NeuroImage*, *34*, 639–650.

Glaunès, J. (2005). *Transport par difféomorphismes de points, de mesures et de courants pour la comparaison de formes et l'anatomie numérique*. Ph.D. thesis Université Paris 13 http://cis.jhu.edu/ joan/TheseGlaunes.pdf.

Glaunès, J., & Joshi, S. (2006). Template estimation from unlabeled point set data and surfaces for computational anatomy. In X. Pennec, & S. Joshi (Eds.), *Proc. of the International Workshop on the Mathematical Foundations of Computational Anatomy (MFCA-2006)*.

Glaunès, J., Qiu, A., Miller, M., & Younes, L. (2008). Large deformation diffeomorphic metric curve mapping. *International Journal of Computer Vision*, *80*, 317–336.

Goodlett, C., Fletcher, P., Gilmore, J., & Gerig, G. (2008). Group statistics of DTI fiber bundles using spatial functions of tensor measures. In *Proc. of MICCAI* (pp. 1068–75). Springer volume 3750 of *LNCS*.

Gorbunova, V., Durrleman, S., Lo, P., Pennec, X., & de Bruijne, M. (2010). Lung CT registration combining intensity, curves and surfaces. In *IEEE International Symposium on Biomedial Imaging* (pp. 340–343).

Jackowski, M., Kao, C. Y., Qiu, M., Constable, R. T., & Staib, L. H. (2005). White matter tractography by anisotropic wavefront evolution and diffusion tensor imaging. *Medical Image Analysis*, *9*, 427 – 440.

Jones, D. K., Griffin, L. D., Alexander, D. C., Catani, M., Horsfield, M. A., Howard, R., & Williams, S. C. R. (2002). Spatial normalization and averaging of diffusion tensor MRI data sets. *NeuroImage*, *17*, 592 – 617.

Joshi, S., & Miller, M. (2000). Landmark matching via large deformation diffeomorphisms. *IEEE Transaction on Image Processing*, *9*, 1357–1370.

Juch, H., Zimine, I., Seghier, M. L., Lazeyras, F., & Fasel, J. H. (2005). Anatomical variability of the lateral frontal lobe surface: implication for intersubject variability in language neuroimaging. *NeuroImage*, *24*, 504 – 514.

Kumar, R., Vemuri, B. C., Wang, F., Syeda-Mahmood, T., Carney, P. R., & Mareci, T. H. (2009). Multi-fiber reconstruction from DW-MRI using a continuous mixture of hyperspherical von Mises-Fisher distributions. In *Proc. of Information Processing in Medical Imaging (IPMI)* (pp. 139–150). Springer volume 5636 of *Lecture Notes in Computer Science*.

Maddah, M., Wells, W. M., Warfield, S. K., Westin, C.-F., & Grimson, W. E. L. (2007). Probabilistic clustering and quantitative analysis of white matter fiber tracts. In *Proc. of IPMI'07* (pp. 372–383). Springer volume 4584 of *LNCS*.

Malcolm, J. G., Michailovich, O., Bouix, S., Westin, C.-F., Shenton, M. E., & Rathi, Y. (2010). A filtered approach to neural tractography using the watson directional function. *Medical Image Analysis*, *14*, 58 – 69.

Mangin, J.-F., Rivière, D., Cachia, A., Duchesnay, E., Cointepas, Y., Papadopoulos-Orfanos, D., Collins, D. L., Evans, A. C., & Régis, J. (2004). Object-based morphometry of the cerebral cortex. *Transactions on Medical Imaging*, *23*, 968–982.

Meyer, Y. (2001). *Oscillating patterns in image processing and nonlinear evolution equations* volume 22 of *University Lecture Series*. Providence, RI: American Mathematical Society. The fifteenth Dean Jacqueline B. Lewis memorial lectures.

Miller, I., M, Trouvé, A., & Younes, L. (2002). On the metrics and Euler-Lagrange equations of Computational Anatomy. *Annual Review of Biomedical Engineering*, *4*, 375–405.

Ochiai, T., Grimault, S., Scavarda, D., Roch, G., Hori, T., Rivière, D., Mangin, J. F., & Régis, J. (2004). Sulcal pattern and morphology of the superior temporal sulcus. *NeuroImage*, *22*, 706 – 719.

Pennec, X., Fillard, P., & Ayache, N. (2006). A Riemannian framework for tensor computing. *International Journal of Computer Vision*, *66*, 41–66.

Savadjiev, P., Campbell, J. S., Descoteaux, M., Deriche, R., Pike, G. B., & Siddiqi, K. (2008). Labeling of ambiguous subvoxel fibre bundle configurations in high angular resolution diffusion MRI. *NeuroImage*, *41*, 58 – 68.

Smith, S., Jenkinson, M., Johansen-Berg, H., Rueckert, D., Nichols, T., Mackay, C., Watkins, K., Ciccarelli, O., Cader, M., Matthews, P., & Behrens, T. (2006). Tract-based spatial statistics: Voxelwise analysis of multi-subject diffusion data. *NeuroImage*, *31*, 1487–1505.

Staempfli, P., Jaermann, T., Crelier, G., Kollias, S., Valavanis, A., & Boesiger, P. (2006). Resolving fiber crossing using advanced fast marching tractography based on diffusion tensor imaging. *NeuroImage*, *30*, 110 – 120.

Trouvé, A., & Younes, L. (2005). Metamorphoses through lie group action. *Foundations of Computational Mathematics*, *5*, 173–198.

Vaillant, M., & Glaunès, J. (2005). Surface matching via currents. In *Proceedings of Information Processing in Medical Imaging (IPMI)* (pp. 381–392). Springer volume 3565 of *Lecture Notes in Computer Science*.

Vaillant, M., Miller, M., Younes, L., & Trouvé, A. (2004). Statistics on diffeomorphisms via tangent space representations. *NeuroImage*, *23*, 161–169.

Vaillant, M., Qiu, A., Glaunès, J., & Miller, M. (2007). Diffeomorphic metric surface mapping in subregion of the superior temporal gyrus. *NeuroImage*, *34*, 1149–1159.

Vercauteren, T., Pennec, X., Malis, E., Perchant, A., & Ayache, N. (2007). Insight into efficient image registration techniques and the demons algorithm. In *Proc. of IPMI'07* (pp. 495–506). Springer volume 4584 of *LNCS*.

Wassermann, D., Bloy, L., Kanterakis, E., Verma, R., & Deriche, R. (2010). Unsupervised white matter fiber clustering and tract probability map generation: Applications of a gaussian process framework for white matter fibers. *NeuroImage*, *51*, 228 – 241.

Yeo, B., Vercauteren, T., Fillard, P., Peyrat, J.-M., Pennec, X., Golland, P., Ayache, N., & Clatz, O. (2009). DT-REFIND: Diffusion tensor registration

with exact finite-strain differential. *Transactions on Medical Imaging*, *28*, 1914–1928.

Zhang, H., Yushkevich, P. A., Rueckert, D., , & Gee, J. C. (2007). Unbiased white matter atlas construction using diffusion tensor images. In *Proc. of MICCAI'07* (pp. 211–218). volume 4792 of *LNCS*.

Ziyan, U., Sabuncu, M. R., O'Donnell, L. J., & Westin, C.-F. (2007). Nonlinear registration of diffusion MR images based on fiber bundles. In *Proceedings of MICCAI'07* (pp. 351–358). volume 4791 of *LNCS*.

Ziyan, U., & Westin, C.-F. (2009). Consistency clustering: A robust algorithm for group-wise registration, segmentation and automatic atlas construction in diffusion MRI. *International Journal Computer Vision*, *85*, 279–290.